Monthly Weather Review

Heavy precipitation over Italy from the Mediterranean storm “Vaia” in October 2018: Assessing the role of an atmospheric river

--Manuscript Draft--

Manuscript Number:	MWR-D-20-0021
Full Title:	Heavy precipitation over Italy from the Mediterranean storm “Vaia” in October 2018: Assessing the role of an atmospheric river
Article Type:	Article
Corresponding Author:	Silvio Davolio Italian National Research Council - CNR Bologna, ITALY
Corresponding Author's Institution:	Italian National Research Council - CNR
First Author:	Silvio Davolio
Order of Authors:	Silvio Davolio
	Stefano Della Fera
	Sante Laviola
	Mario Marcello Miglietta
	Vincenzo Levizzani
Abstract:	The Mediterranean storm “Vaia” developed within a typical autumn synoptic circulation, generally associated with heavy rain conditions over the western Mediterranean basin. Intense precipitation was responsible for floods over Italy between 27-30 October 2018 and the storm was accompanied by explosive cyclogenesis, storm surge and extremely intense wind gusts, that caused casualties and extensive damages, especially to the Alpine forests. This study investigates the contribution of different moisture sources to the extreme precipitation by means of numerical model simulations using the Bologna Limited Area Model (BOLAM). In particular, the attention is focused on the significant amount of water vapor transported into the Mediterranean basin from the Atlantic tropical area, and organized along a narrow corridor across the African continent. First, a newly developed detection algorithm is applied to identify this transport as an Atmospheric River (AR). Then, the implementation of an atmospheric water budget diagnostic, supported by sensitivity experiments, allows to assess the role of the AR in terms of water supply to the precipitation systems. Although the transport of moisture from remote regions is known to be an important ingredient for the onset of heavy precipitation in the Mediterranean, the role of ARs, already identified in correspondence with some of these events, has not been deeply investigated and quantified yet in this specific area. The results demonstrate that the AR was critical for determining the magnitude of this heavy precipitation episode over Italy, while evaporation from the sea played a secondary role, especially for precipitation over the Alps.

Heavy precipitation over Italy from the Mediterranean storm "Vaia" in October 2018: Assessing the role of an atmospheric river

S. Davolio[1], S. Della Fera[2], S. Laviola[1], M. M. Miglietta[3] and V. Levizzani[1]

[1] Institute of Atmospheric Sciences and Climate, National Research Council, CNR-ISAC, Bologna, Italy

[2] Department of Physics and Astronomy, University of Bologna, Italy

[3] Institute of Atmospheric Sciences and Climate, National Research Council, CNR-ISAC, Padova, Italy

Corresponding author: Silvio Davolio, S.Davolio@isac.cnr.it

Submitted to *Monthly Weather Review* - January 2020

Revision submitted in June 2020

Abstract

The Mediterranean storm “Vaia” developed within a typical autumn synoptic circulation, generally associated with heavy rain conditions over the western Mediterranean basin. Intense precipitation was responsible for floods over Italy between 27-30 October 2018 and the storm was accompanied by explosive cyclogenesis, storm surge and extremely intense wind gusts, that caused casualties and extensive damages, especially to the Alpine forests. This study investigates the contribution of different moisture sources to the extreme precipitation by means of numerical model simulations using the Bologna Limited Area Model (BOLAM). In particular, the attention is focused on the significant amount of water vapor transported into the Mediterranean basin from the Atlantic tropical area, and organized along a narrow corridor across the African continent. First, a newly developed detection algorithm is applied to identify this transport as an Atmospheric River (AR). Then, the implementation of an atmospheric water budget diagnostic, supported by sensitivity experiments, allows to assess the role of the AR in terms of water supply to the precipitation systems.

Although the transport of moisture from remote regions is known to be an important ingredient for the onset of heavy precipitation in the Mediterranean, the role of ARs, already identified in correspondence with some of these events, has not been deeply investigated and quantified yet in this specific area. The results demonstrate that the AR was critical for determining the magnitude of this heavy precipitation episode over Italy, while evaporation from the sea played a secondary role, especially for precipitation over the Alps.

1. Introduction

Between 27 and 30 October 2018 the Italian peninsula was affected by an intense cyclone, named “Vaia” by the Free University of Berlin, that caused extraordinary severe weather. Heavy precipitation occurred in several areas causing floods and landslides. The fierce winds led to destructive waves and storm surges (Cavaleri et al. 2019; Magnusson and Cavaleri 2019) in both the Ligurian and the Adriatic Sea (the water level in Venice ranked fourth in history), as well as to extensive (41000 ha) forest damages, resulting in the loss of about 8 million m^3 of trees in the north-eastern Alpine region, the worst wood destruction in Italy of all times (Motta et al. 2018).

The synoptic characteristics leading to the storm development were those typical of autumn intense Alpine precipitation events, widely investigated in the last decades during research programs as the Mesoscale Alpine Programme (MAP, Bougeault et al. 2001), the MEDiterranean EXperiment (MEDEX, Jansa et al. 2014) and the Hydrological cycle in the Mediterranean eXperiment (HyMeX, Drobinski et al. 2014). Such events are characterized by a pronounced large-scale trough, which slowly evolves eastward over the western Mediterranean basin (Grazzini 2007). However, the Vaia event turned out to be exceptional, not only in terms of wind and cumulated precipitation (up to 850 mm in three days, return period exceeding 100 years; ARPAV 2018), but also of integrated water vapor (IWV) transported over the Mediterranean, as recently shown in Grazzini et al. (2019), who classified the storm as likely one of the strongest ever recorded in Italy.

The organization of the large-scale flow (Fig. 1), associated with the development of a large amplitude baroclinic wave, set the conditions for the onset of an intense meridional exchange, advecting moisture from the Mediterranean basin towards the Alps for several days. Moisture availability and transport are key factors for heavy precipitation and flood events in the Mediterranean (Khodayar et al. 2018), particularly over Italy, as demonstrated in many studies (Reale et al. 2001; Turato et al. 2004; Bertò et al. 2004; Martius et al. 2008; Winschall et al. 2012; Pinto et al. 2013). Moreover, the partitioning of moisture supply between local (Mediterranean Sea surface evaporation) and remote sources was investigated in recent studies. Duffourg and Ducrocq (2011, 2013) analyzed the origin of moisture feeding precipitation systems in southeastern France and concluded that evaporation from the Mediterranean Sea is the main source (> 50%) only when anticyclonic conditions prevail in the days before the event. For high-impact southern Alpine precipitation, the outcomes are highly variable on an event basis. Winschall et al. (2012, 2014) identified evaporation and transport from the North Atlantic as major contributions, especially for orographic precipitation, in agreement with Turato et al. (2004) and Rudari et al. (2005). Pinto et al. (2013) demonstrated the role of large-scale moisture advection from the North Atlantic basin; the latter becomes increasingly important with the increase in rainfall amount over north-western Italy, especially in winter. Finally, the highly variable contribution of Mediterranean and extra-Mediterranean moisture sources was deeply analyzed by Krichak et al. (2015, 2016), who identified also the important role of moisture sources in the subtropics for a significant number of extreme precipitation events in the basin.

It is well known that a large fraction of moisture moves from the tropics to mid-latitudes within long and narrow filament-shaped structures of strong horizontal water vapor transport called Atmospheric Rivers (AR), typically associated with a low-level jet stream ahead of the cold front of an extratropical cyclone (Zhu and Newell 1998; Dacre et al. 2015; Ralph et al. 2018). ARs can be responsible of heavy precipitation where they make landfall and are forced to rise above a mountain chain (Gimeno et al. 2014).

Although most of the literature on ARs in the past decades was devoted to study moist processes, climatology and impacts on the US west coast (Neiman et al. 2011; Ralph and Dettinger 2011; Rutz et al. 2014; Ralph et al. 2019), more recently the topic gained attention also for Europe. The formation of ARs over the Atlantic Ocean was documented by Knippertz and Wernli (2010), and a strong link with heavy precipitation over western Europe was demonstrated by Lavers and Villarini (2013). The Iberian Peninsula (Liberato et al. 2012; Ramos et al. 2015), the UK and France (Lavers et al. 2011; Browning 2018), and the Scandinavian Peninsula (Sodemann and Stohl 2013; Benedict et al. 2019) experienced the effects of ARs on the windward slopes of mountain ranges, which provided the necessary uplift for the condensation of the impinging water vapor. In the Mediterranean basin, and in Italy in particular, the role of ARs in severe weather has been scarcely investigated. A few studies suggested a link between extreme precipitation events over Italy and the possible occurrence of ARs (Bertò et al. 2004; De Zolt et al. 2006; Malguzzi et al. 2006; Buzzi et al. 2014), but only Krichak et al. (2015) applied specific diagnostics to assess the role of an AR during the historical 1966 flood in Florence, indicating the central and eastern tropical North Atlantic as the main source of humid air.

Within this framework, the present study aims at identifying the presence of an AR associated with the Vaia storm and at assessing its role in modulating the intense precipitation over both northern and central Italy. The investigation is mainly performed through numerical simulations undertaken with the mesoscale model BOLAM (BOlogna Limited Area Model), implementing an atmospheric water budget computation procedure.

The main meteorological aspects of the storm are described in Section 2, while the experimental design and the diagnostic tools are introduced in Section 3. Section 4 presents the simulation results and the detection of the AR. The role of the AR is discussed in Section 5, where the atmospheric water budget is computed and sensitivity experiments are presented. Finally, conclusions are drawn in Section 6.

2. Meteorological features of the Vaia storm

Between 26 and 27 October 2018, a mid-tropospheric trough began to deepen over western Europe, elongating from Scandinavia all over France and the Iberian Peninsula. The trough was accompanied by cold air advection in the mid-troposphere (Fig. 1a), while surface cyclogenesis took place over the western Mediterranean. Simultaneously, a pressure ridge reinforced over eastern Europe, so that the whole picture appeared as an intensifying baroclinic wave slowly moving eastward. During 27 and 28 October (Fig. 1b), the trough further extended over northern Africa, associated with a narrow and longitudinally elongated positive potential vorticity (PV) pattern in the high troposphere, as often occurs during Mediterranean extreme events (Massacand et al. 1998). The trough axis slightly rotated counterclockwise, while the warm front lied almost stationary along the Alpine crest (see also the animation of 500 hPa geopotential height, PV at 300 hPa and fronts in the supplemental material). The intense warm and moist meridional flow impinged directly on the Italian orography, conveying large amounts of moisture towards the Apennines and the central/eastern Alps. At the mesoscale, as usually occurs in the presence of this large-scale circulation, meridional flows in the lower troposphere progressively intensified and rotated from south-westerly to south-easterly, while low-level jets developed over both the Tyrrhenian and the Adriatic Sea (Sirocco conditions, shown by the wind field at 950 hPa in the supplemental material). This set-up produced the first phase of intense precipitation, which was mainly associated with nearly moist neutral flow rising over the Italian orography, as revealed for example by the radiosoundings in Udine (not shown). Rainfall was mainly stratiform, with some embedded convection (as demonstrated by the low number of recorded lightning strikes), moderate in intensity but persistent, since under nearly moist adiabatic lifting its intensity depends upon the strength of the impinging flow (Miglietta and Rotunno 2006) and the transported moisture (Malguzzi et al. 2006). In details, precipitation amounts (Fig. 2a) reached locally up to 500 mm in 48 h over the north-eastern Alps, where snowfall was confined at high elevation (above 2000–2500 m) for most of the time, as a consequence of the warm air advection. Over the Apennines of Liguria and central Italy, rainfall exceeded 400 and 250 mm in 48 h, respectively.

After a temporary cessation of precipitation activity in the night of 28 October, a second phase of even more intense rainfall took place on 29 October, when the cold front entered the Mediterranean basin (Fig. 1c and 1d). The environment was strongly baroclinic, with an evident westward tilting of the trough axis and the jet stream maximum moving over the basin (see the animation of wind at 300 hPa in the supplemental material); the sharp contrast between the incoming cold air and the air masses present over the sea, whose water temperature was characterized by a relevant warm anomaly (between 1 and 3 K over the western Mediterranean), rapidly intensified the low-level cyclogenesis.

The evolution of the surface low, initially characterized by several pressure minima slightly below 1000 hPa, underwent an explosive deepening (Sanders and Gyakum 1980), with a drop of 20 hPa in 18 h. In the morning, the cyclone developed offshore the Tunisian coast; at 1200 UTC, a 985 hPa cyclone was located between Sardinia and the Balearic Islands, and later in the evening it moved over north-western Italy, further intensifying (up to 977 hPa) and contracting its horizontal scale (Fig. 1d). The mid-tropospheric trough shifted eastward (Fig. 1c) and contributed, together with the abrupt cold air entrance (Mistral over the Gulf of Lion), to trigger intense mesoscale convective systems over the Tyrrhenian and Ligurian Seas. At the same time, over the Alps convective activity became more pronounced with higher rainfall rates (convection is clearly shown by MODIS image and satellite animation in the supplemental material). By 30 October, 0000 UTC the cold front had already swept the Adriatic basin, while the surface cyclone crossed the Alps.

It is worth mentioning that, in the evening of 29 October, the sharp pressure gradient across the Po Valley, due to the passage of the cyclone, contributed to reinforce the synoptically driven Sirocco wind over the Adriatic. Together with the squeezing of the Sirocco against the Dinaric Alps (due to cold air from the Tyrrhenian Sea that crossed the northern Apennines and spilled over the Adriatic basin; Cavaleri et al. 2019 and 10-m wind shown in the supplemental material), the pressure gradient was responsible for the exceptional wind storms (and consequently waves and surge) experienced over north-eastern Italy, where gusts exceeding 200 km h^{-1} were recorded.

Rainfall (Fig. 2b), mainly originated from deep convection, was associated with a remarkable lightning activity and showers that produced 250–300 mm in less than 24 h in the eastern Alpine regions, about 200 mm in Liguria and more than 100 mm in several areas of central Italy.

Therefore, during three days, rainfall maxima ranged between 600 mm in the central Alps and almost 900 mm in the eastern Alps, exceeding 600 mm in Liguria and 400 mm in central Italy. For several Alpine areas, this was the strongest event of the last 150 years in terms of rainfall and wind intensity.

3. Experimental design

a. The NWP model BOLAM

BOLAM is a hydrostatic limited-area model, which integrates the primitive equations on a latitude-longitude rotated grid. The model prognostic variables are distributed in the vertical on a regular Lorenz grid, while the horizontal discretization is based on a staggered Arakawa C grid. BOLAM uses a hybrid vertical coordinate system, in which the terrain-following coordinate σ ($0 < \sigma < 1$) smoothly tends to a pressure coordinate with increasing height above the ground. The temporal integration scheme is split-explicit and forward–backward for the gravity modes. Three-dimensional advection is computed based on a second-order, weighted-average flux implementation with "superbee" limiter (Hubbard and Nikiforakis 2003). To maintain numerical stability and prevent build-up of energy at the smallest scales, diffusion and filters are applied. For further details on BOLAM see Buzzi et al. (2003, 2014).

BOLAM physics includes convection, atmospheric radiation, turbulence, soil processes and microphysics. The parameterization of the atmospheric convection is based on a modified version of the Kain (2004) scheme. The atmospheric radiation is computed through a combined application of the Ritter and Geleyn (1992) and the ECMWF schemes (Morcrette et al. 2008). The turbulence scheme is based on an eddy kinetic energy–mixing length (E–l), 1.5-order closure theory, where the turbulent kinetic energy equation (including advection) is predicted (Zampieri et al. 2005). The soil model uses seven layers, and it takes into account the observed geographical distribution of different soil types, vegetation coverage and soil physical parameters. It computes surface energy, momentum, water and snow balances, heat and water vertical transfer, vegetation effects at the surface and in the soil. A simple slab ocean model evolves the sea surface temperature depending on radiative and latent/sensible heat surface fluxes. The microphysical processes are treated with a simplified approach, suitable for non-convection-resolving models, based on the parametrization proposed by Drofa and Malguzzi (2004) that describes the conversions and interactions of cloud water, cloud ice and hydrometeors (rain, snow and graupel). Finally, a simple gravity orographic wave drag parameterization has been introduced. BOLAM has been largely validated and compared with other mesoscale models for application to heavy precipitation events in the course of international projects (Anquetin et al. 2005; Mariani et al. 2005; Davolio et al. 2013; Buzzi et al. 2014).

In the present study, the BOLAM integration domain covers a wide area, including Europe and a large portion of the Atlantic Ocean even at low latitudes (Fig. 3), with a grid spacing of about 10 km and 50 vertical levels. Initial and boundary conditions for BOLAM are provided by 6-hourly IFS-ECMWF analysis fields and imposed through a relaxation scheme. Simulations are initialized at 1200 UTC, 26 October 2018. For the sensitivity experiments described in Section 5b, the BOLAM domain is reduced in latitude since the southern (northern) boundary is moved northward (slightly southward) (Fig. 3).

b. Water budget computation and water supply to heavy rainfall

In order to evaluate the water supply to heavy precipitation, a methodology is developed for the computation of the water budget within an atmospheric box, suitably located over the Mediterranean basin upstream of the precipitation area. Moreover, the procedure allows to assess the relative importance of sea evaporation with respect to remote moisture sources. The diagnostic tool is similar to that presented in Davolio et al. (2017), except that the contributions to the water budget are computed as fluxes across the box walls instead of being converted into energy units. A similar methodology was also applied by Duffourg and Ducrocq (2013) in order to identify different moisture sources for heavy precipitation events over south-eastern France.

The variation of the total atmospheric water in the box (ΔIW) can be ascribed to evaporation (E) from the surface and precipitation (P), and to horizontal fluxes (F) across each side of the box:

$$\Delta \mathrm{IW} = \mathrm{E} - \mathrm{P} + \mathrm{F} + \mathrm{Res} \qquad (1)$$

Positive (negative) fluxes indicate inflow (outflow). The first two contributions are a direct output of the model, since the bottom side of the box is defined at the model surface. The residual term accounts for numerical errors and approximations in the computation of the budget due to interpolations, time discretization and comparison of the instantaneous fluxes computed on the lateral sides with the integral values (accumulated over prescribed time interval) at the bottom, provided directly by the BOLAM model. In order to minimize these inaccuracies and to consider the typical short time scale of microphysical/precipitation processes occurring inside the box, the computation is performed every 15 min (corresponding to 9 model time steps).

Instantaneous meridional water fluxes across each of the two lateral walls are obtained as

$$F_m = \int_{z_i}^{z_f} \int_{x_i}^{x_f} \rho_v \, V \, dx \, dz \qquad (2)$$

where ρ_v is the vapour density, defined from the specific humidity q that includes all the different water species, namely vapor, water and ice, as $\rho_v = \rho_{air}\, q$, and V is the normal wind component. Using the hydrostatic equation, the flux can be expressed in terms of BOLAM longitude-latitude rotated coordinates (λ, ϕ), with σ = vertical coordinate, a = Earth radius and g = gravity

$$F_m = -\frac{a}{g} \int_{\sigma_i}^{\sigma_f} \int_{\lambda_i}^{\lambda_f} q \, V \, cos\phi \, d\lambda \, \frac{dp}{d\sigma} d\sigma \qquad (3)$$

Similarly, zonal water fluxes across the two meridional walls of the boxes are computed as

$$F_z = -\frac{a}{g} \int_{\sigma_i}^{\sigma_f} \int_{\phi_i}^{\phi_f} q \, U \, d\phi \, \frac{dp}{d\sigma} d\sigma \qquad (4)$$

E and P are computed at the bottom of the box. Since they are both provided by the model as integral values, they must be referred to an instantaneous rate, which is calculated assuming a linear variation during the considered 15-min window. Moreover, to compute E, cumulated surface latent heat fluxes are converted into mass fluxes, using the latent heat of evaporation.

Finally, the integrated water in the box is computed at the analysis time step as

$$IW = \frac{a^2}{g} \int_{\lambda_i}^{\lambda_f} \int_{\phi_i}^{\phi_f} \int_{\sigma_f}^{\sigma_f} q \, cos\phi \, d\lambda \, d\phi \, \frac{dp}{d\sigma} d\sigma \tag{5}$$

and ΔIW is simply the difference between IW at two consecutive steps.

First, the correct closure of the atmospheric water budget is verified within a box centered over the western Mediterranean (Fig. 3), extending from the surface up to 300 hPa. At this elevation, outgoing contribution at the top can be considered negligible. The residual term is always at least one order of magnitude lower than the others, therefore it is small enough to ensure a correct use of this diagnostic tool. Since we are interested in the transport of moisture in the lower troposphere, the water budget terms are then computed and analyzed in a box extending up to 700 hPa.

The water budget can be also exploited to evaluate the relative contribution of remote/local moisture sources (where "local" means evaporation from the Mediterranean) feeding the precipitation. To this aim, a procedure similar to Duffourg and Ducrocq (2013) is applied. First, the periods of precipitation, between t_{ini} and t_{fin}, are identified for the region of interest. Then, analyzing the wind field in the lower troposphere, it is possible to estimate the time (Δt_i, i indicates a specific time) a parcel takes to travel from the budget box to the rainfall area. Therefore, during the period between t_{ini}-Δt_1 and t_{fin}-Δt_2, the air masses that will feed precipitation emerge from the northern section of the box. If Δt_{box} is an estimate of the time required to cross the box, then [t_{ini}-Δt_1-Δt_{box1}; t_{fin}-Δt_2-Δt_{box2}] defines the time interval during which the air masses that will feed the precipitation system enter the budget box. During this period, positive fluxes across a box side provide an indication about the region of origin of the moisture. Thus, integrating in time the ingoing fluxes F, it is possible to estimate the mass of water that will supply the downstream rainfall. Similarly, the time integration of the sea evaporation during the period [t_{ini}-Δt_1-Δt_{box1}; t_{fin}-Δt_2] allows to evaluate the local contribution to heavy precipitation.

4. Analysis of the control simulation

First, the simulation was validated through comparison between model output and observations. For this purpose, rainfall, wind and temperature data from the National Civil Protection Department and regional networks were used. Moreover, several technical reports of the event, available from the meteorological centers of the regions affected by the storm, were exploited to assess the ability of the simulation to correctly reproduce the main dynamical patterns of the event and the spatial and temporal distribution of precipitation. A detailed assessment of model performance is out of the scope of the present paper; however, the simulation turned out to be in a reasonably good agreement with the observations, as shown for example in Fig. 4: although BOLAM underestimates the total amount of precipitation, it correctly reproduces the spatial distribution and the temporal evolution of rainfall (cfr. with Fig. 2). It is worth noting that the simulated amount of precipitation is extreme anyway; hence, the run successfully reproduces the exceptional character of the event, especially bearing in mind the limitation of a hydrostatic model implemented at a moderate resolution. Therefore, this simulation is considered suitable for performing deeper diagnostic analyses and can therefore serve as reference for sensitivity experiments.

The analysis of the IWV fields (integrated from 1000 to 300 hPa) allows to further validate the simulation and to identify the main regions where vapor is transported during the event. At 1200 UTC, 27 October 2018, the predicted IWV shows three areas characterized by high amounts of moisture (Fig. 5a), one located over the Atlantic Ocean and the western Mediterranean Sea, another over the tropical Atlantic and western Africa, the latter over the southern Mediterranean and Libya.

These patterns are in good agreement with the total precipitable water retrieved from satellite (Wimmers and Velden 2011), both in terms of location and amount (Fig. 5g). However, in order to have a complete picture of the dynamics, it is necessary to consider the Integrated Vapor Transport (IVT) computed over the same depth of atmosphere as well as the IWV (Fig. 5d). On the eastern border of the high pressure located over the North Atlantic (see Fig. 1a), the pressure gradient generates intense southward cold air advection. Southerly wind sharply diverges offshore the Iberian Peninsula (as shown by the IVT in Fig. 5d). This pattern forces part of the moist air masses over the Atlantic to enter the Mediterranean basin in correspondence of the Gibraltar Strait and to flow north-eastward towards Italy. On the other hand, the tropical moisture over Libya is not markedly affecting the western and central Mediterranean basin, since the northward transport is relatively weak and progressively moves eastward, as evident 24 h later (Figs. 5b,e,h). Finally, the transport of moisture directed towards the Mediterranean becomes organized from the tropical Atlantic Ocean through the African continent, driven by the large-scale trough deepening over the Iberian Peninsula. This latter corridor of moisture transport becomes the main feature during 28 and 29 October (Figs. 5c,f,i), since the Atlantic injection into the Mediterranean appears cut off at this time. Although the IWV evolution (Figs. 5a-c) may give the impression that the AR is formed by the convergence of the three regions of enhanced moisture (shown in Fig. 5a) and that it does not represent a coherent meridional transport feature, the IVT maps (Figs. 5d-f) do provide some hints that this is not the case. However, in order to banish all doubts, back-trajectories are computed using the HYSPLIT model (Stein et al. 2015; Rolph et al. 2017) driven by GFS data. Analyzed back-trajectories (not shown) depart from the two rainfall areas (northern and central Italy) at different times of the precipitation days and from different elevations in the lower-middle troposphere, thus sampling the precipitation systems. The analysis confirms that, besides the contribution from the Atlantic to the precipitation over northern Italy during the first day (27 October) of the event, the moisture transport towards the Italian peninsula occurs primarily in an AR that conveys air-masses from tropical areas. The model simulation is in very good agreement with satellite product of total precipitable water displayed in Figs. 5g-i showing a progressive intensification of IWV over the Saharan desert and over the Mediterranean. Here, the highest values of IVT are associated with the low-level jet located ahead of the approaching cold front (a snapshot of the low-level jet ahead of the front is provided by 950 hPa wind and equivalent potential temperature fields in the supplemental material).

a. Atmospheric river detection

The IWV and IVT maps simulated by BOLAM (Figs. 5a-f) reveal the presence of a narrow corridor of water vapor moving from the tropical Atlantic to the Mediterranean. In order to define this pattern as an AR, the simultaneous verification of geometric and dynamic criteria has to be satisfied, as indicated in the literature (e.g., Ralph et al. 2004; Gimeno et al. 2014; Rutz et al. 2014): narrow zones about 2000 km long and 300–500 km wide (ratio length/width > 2), with an IWV greater than 2.0 cm and IVT greater than 250 kg m^{-1} s^{-1}. Moreover, a scale has also been recently introduced by Ralph et al. (2019) to characterize the intensity of ARs on the basis of the maximum IVT value and of the event duration. For a given duration (e.g., 24-48 hours), the intensity thresholds are: weak (250–500 kg m^{-1} s^{-1}), moderate (500–750 kg m^{-1} s^{-1}), strong (750–1000 kg m^{-1} s^{-1}) and extreme (> 1000 kg m^{-1} s^{-1}). Although these magnitude thresholds are a handy tool for defining the AR intensity, recent studies additionally consider the duration of AR conditions at landfall. Some heavy flooding events over the US have shown that stronger and more persistent IVTs (> 48 h) are associated more frequently with hazardous impacts than weaker and less persistent ARs. Therefore, a robust classification of the AR intensity is provided by the combination of the IVT instantaneous magnitude and the duration of AR conditions as described in Ralph et al. (2019).

An algorithm has been developed and applied to the model output in order to identify the contiguous grid points where both IWV and IVT exceed the above-mentioned thresholds at a given time. This procedure defines an object, that is an area that can be classified as an AR if the geometrical requirements are satisfied. Applying this algorithm to the BOLAM output fields, an AR is clearly identified during 28 and 29 October (Fig. 6a). It is about 3000 km long and 500 km wide, extending from Africa tropical areas to the Mediterranean. To better characterize the AR, several vertical cross sections of water vapor flux and normal wind speed were drawn across north Africa (Fig. 6b). Around 30°N latitude, just north of the Sahara, moisture is confined below 700 hPa, and the transport of water vapor is strongly correlated with the maximum wind velocity, positioned between 800–700 hPa. Note that while for the US west coast the ARs move over the Pacific Ocean, in this case the AR propagation occurs over land, before it emerges into the Mediterranean basin. In spite of this remarkable difference, the same threshold parameters allow the formal identification of the AR. The AR can be classified as “extreme” on the basis of the AR intensity scale described above, since the simulated IVT slightly exceeds 1500 kg m^{-1} s^{-1}, with a duration longer than 24 h. The amount of water transported by the AR across a vertical section 50 km wide in the Mediterranean can be easily estimated, and during the most intense phase attained an impressive value of about 5×10^7 kg s^{-1}, i.e. several time the discharge of the Po river (northern Italy) during a flood.

5. Role of the AR

Since the presence of an AR is clearly demonstrated, the next step is to quantify its role on the heavy precipitation event in different regions of the Italian peninsula. In particular, the investigation is focused on two areas: northern Italy, broadly defined as an area encompassing both the central/eastern Alps and northern Apennines, where the time evolution of precipitation was similar, and central Italy (Figs. 7a,c). Over these two regions, the area-averaged precipitation is computed hourly from the BOLAM output and shown in Fig. 7b,d. Over northern Italy, the two periods of precipitation described in Section 2 clearly emerge, with a break in between. Instead, over central Italy, the pattern is more complex, probably due to convective activity moving inland from the Tyrrhenian Sea, and three different rainfall intervals can be identified. For each of these precipitation phases, t_{ini} and t_{fin} are defined to carry out the diagnostic analysis as described in Section 3b.

a. Water budget analysis

The first step for the computation of the atmospheric water budget is to define a suitable box, upstream of the precipitation area, able to intercept the main flows contributing to feed the precipitation system. For rainfall over northern Italy, bearing in mind the IVT maps analyzed in the previous section, it is necessary to define a wide budget box (Fig. 3), in order to consider both the southerly flow possibly associated with the arrival of the AR, and the contribution initially coming from the Atlantic Ocean, just south of the Iberian Peninsula.

Figure 8a shows the time evolution of the different terms of the water budget, that is the incoming/outgoing fluxes across the four lateral sides, evaporation and precipitation through the bottom face, as described in Section 3b. Overall, the budget is dominated by a symmetry between the incoming (positive) and outgoing (negative) fluxes across the southern and the northern sides of the box, respectively. However, during the first 24–36 h, approximately until 0000 UTC, 28 October, the flux across the western section is also relevant and reveals the contribution coming from the Atlantic, previously identified in Figs. 5a,d,g. Incoming meridional fluxes progressively increase during the first phase of the event. However, during 27 October, while the southerly contribution further intensifies and reaches a peak associated with the arrival of the AR over the Mediterranean, the westerly contribution remains almost constant before decreasing by the end of the day, as a consequence of the cut-off of the Atlantic inflow into the Mediterranean described above. During 28 October, the largely predominant positive contribution to the water budget can be ascribed to the AR entering the southern side of the box (shown in Fig. 3), which reaches a peak of about 3×10^8 kg s^{-1} in the evening of 28 October, at around 1800 UTC. However, the outgoing flux across the northern side does not show a corresponding peak. This is partially due to the effect of precipitation occurring over the sea, but also to the intense low-level north-westerly flow, driven by the Mistral, which produces a positive (incoming) contribution across the northern section in its westernmost portion since the morning of 28 October. Therefore, to better disentangle and highlight the influence of the AR during the second phase of the event (29 October), when the transport is much more confined to the central Mediterranean (as shown in Figs. 5c,f,i), a smaller box is defined (Fig. 7a). The atmospheric water budget within this new box (Fig. 8b) still reveals the westerly Atlantic contribution that crosses the western section between 0000 and 1200 UTC, 28 October (as shown also in Figs. 5d,e). Note that although the two longitudinal sections are now much smaller with respect to the previous box (and even much smaller than the other two sections), the balance, which is expressed in kg s^{-1}, is still dominated by the meridional transport. Without the contribution of the Mistral, the outgoing flux across the northern section reaches almost the same value (3×10^8 kg s^{-1}) as in the previous box, even though the section area is smaller. Thus, the critical contribution of the AR is even more clear, especially after 1200 UTC, 28 October.

The identification of the two rainfall periods for the northern Italy area (Fig. 7b) allows to define the time intervals for the integration of the horizontal fluxes and of evaporation (Figs. 8a,b) (see Section 3b), in order to calculate the relative contribution of local and remote moisture sources. The results are shown in Table 1, where the contributions are computed with respect to the total mass of water entering the box. Remote sources account for almost 80% of the water mass, while evaporation is responsible for the remaining 20%, during the first phase of rainfall (27–28 October).

For the second precipitation phase, occurring mainly on 29 October, the contribution of moisture associated with the meridional transport is even more relevant, while the impact of local evaporation seems to play a minor role in terms of supply to heavy precipitation. This suggests a possible critical role of the AR in feeding the precipitation systems.

The same analysis is performed for the investigation of water supply to heavy rainfall in central Italy. This area is constantly affected by meridional flow impinging the Apennines for almost the entire duration of the event, confined in a limited portion of the Tyrrhenian Sea. Therefore, it is possible to define an atmospheric box for the computation of the budget (Fig. 7c), suitable for all the three phases of rainfall (Fig. 7d). Although the longitudinal sections are much smaller than the meridional sides, the incoming southerly contribution dominates the budget (Fig. 9). The westerly transport is comparable to the meridional one only at the beginning of the event during 27 October, and in the final phase, when the passage of the cold front abruptly changes the direction of the main flows, as evident just after 1200 UTC, 29 October. A sudden increase of the contribution across the southern section, possibly revealing the arrival of the AR, is shown in the afternoon of 27 October, after 1800 UTC.

The time integration of the contributions defines the relative importance of remote transport with respect to local evaporation, as summarized in Table 2. The contribution of meridional transport dominates the amount of water mass entering the box and then feeding the precipitation. The role of the AR seems even more critical here, already at the beginning of the event. Evaporation accounts only for a small portion of water supply, increasing in the final phase of the event, probably due to strong winds associated with the low-level jet ahead of the cold front and intense air-sea interactions.

Therefore, the computation of the atmospheric water budget and the estimation of water supply to heavy precipitation in both target areas display a dominant role of meridional transport from remote regions with respect to local evaporation. Transport from the mid-latitude Atlantic area is relevant only at the beginning. Instead, the presence of the AR, as revealed by the diagnostic detection in Section 4a, and its contribution to the water budget seem to emerge as key factors for this extreme rainfall over Italy. Further numerical experiments have been performed to better define and confirm the role of the AR.

b. Sensitivity numerical experiments

Some additional numerical experiments (Table 3) have been devised to evaluate the sensitivity of the simulation results to the amount of moisture provided by the transport towards the Mediterranean due to the AR and by evaporation from the Mediterranean Sea.

In order to perform the first sensitivity experiment, a preliminary step is required. As clearly shown in Fig. 5, the AR is almost entirely responsible for the northward transport of water vapor south of 30°N. If the southern boundary of the BOLAM integration domain is placed at this latitude, it intercepts entirely the AR moisture transport. Therefore, it becomes very simple to modify this meridional transport in a numerical experiment acting on the boundary condition. However, one must first assess that the results obtained so far in the control simulation (described in Section 4) do not change substantially adopting the new smaller integration area (Fig. 3). A comparison between the simulations performed on the two different domains reveals only minor differences, mainly related to the fine-scale structure of the deep Mediterranean cyclone developed during 29 October, and in particular the rainfall over the two target areas does not present any relevant difference in terms of location and timing. Therefore, these results still hold for the new simulation, which is now taken as reference (REF, Table 3) for the sensitivity experiments.

In the first sensitivity experiment (SBND) the AR contribution is neglected. This is attained by reducing the moisture entering the integration domain across the southern boundary. Since the nesting procedure implies that the global model fields are imposed at the boundaries to force the mesoscale model (boundary condition updating), the experiment consists in a 75% reduction of the amount of humidity in the global model fields only in correspondence of the southern boundary of the BOLAM domain. In terms of pressure fields, this produces only minor modifications to the Mediterranean cyclone depth, since its minimum pressure, after the rapid intensification phase on 29 October, is only approximately 3 hPa weaker than in the REF simulation. However, also the timing of cyclone evolution is slightly changed and the minimum mean sea level pressure is attained a few hours before, so that comparing the two simulations (REF and SBND) at the same time shows even a 6-7 hPa difference due to the time shift. This result suggests that other mechanisms besides diabatic forcing may have contributed to the explosive cyclogenesis, possibly a strong upper air forcing associated with PV anomaly and jet-stream. On the other hand, the impact on rainfall is much more relevant (Fig. 10). In details, over northern Italy (Fig. 10a) the first rainfall phase is almost unchanged. Thus, the moisture coming from the Atlantic and the humidity already present on the Mediterranean, together with the local evaporation, are enough to feed the precipitation systems over northern Italy. However, the sensitivity experiment (SBND) shows a much weaker precipitation on 29 October. Thus, to sustain the second intense rainfall phase, the contribution of moisture reaching the Mediterranean through the AR is critical, except during the last hours, when the passage of the cold front is able to directly trigger convective precipitation. Figure 11 clearly shows the critical drop of moisture transport over the Tyrrhenian Sea towards northern Italy at 0000 UTC, 29 October, that explains the rainfall decrease in the SBND experiment. In fact, this corresponds to the time of maximum meridional moisture flux (Fig. 9b) across the southern and northern section of the box (drawn for clarity also in Fig. 11).

On the other hand, the precipitation field of the SBND sensitivity simulation is dramatically different for central Italy (Fig. 10b) and clearly indicates the important role played by the AR during the entire event. Rainfall is produced only at the very beginning and in the final phase, when it is again associated with the cold front, but most of the precipitation does not occur without the direct contribution of the AR. In fact, this area is more exposed to moist southerly air flows. This result agrees with the water budget outcomes, confirming the AR as a key ingredient for the extreme precipitation. Figure 11 highlights the weak transport of moisture directed towards the central Apennines in the SBND experiment.

Other sensitivity experiments have been performed to better assess the role of the evaporation from the sea. In the first experiment (NOFL, Table 3) surface latent heat fluxes have been turned off during the entire simulation all over the Mediterranean Sea, thus neglecting the local source of humidity. The impact of surface fluxes on area-averaged precipitation is weak over northern Italy (not shown), much smaller than that observed in the previous sensitivity experiment (SBND). The precipitation evolution remains very close to the reference experiment and the area-averaged amount decrease never exceeds 20% during the most intense periods.

On the other hand, the impact is more relevant over central Italy. As shown in Fig. 12, the lack of evaporation from the sea surface is responsible for a considerable decrease of precipitation amount. Although the impact is weaker than that obtained neglecting the AR (Fig. 10b), rainfall is almost halved in the first and in the last phase of the event. During the central phase, when the AR is directly affecting the area, the impact of surface evaporation is more limited.

Another similar sensitivity experiment (NOFL48, Table 3) is performed, turning off latent heat fluxes only after 48 hours of simulation. Since neglecting surface fluxes has an impact on the simulated general meteorological evolution (also due to indirect or non-linear effects, especially for long integration ranges), this simulation allows to keep the evolution unchanged during the first phase of the event and thus to evaluate more neatly the role of surface evaporation in the last period (29 October). Figure 12 confirms the importance of moisture from the Mediterranean Sea for the precipitation over central Italy, while the results do not change over the northern Italy area (not shown). Although the moisture transported by the AR is confirmed as the main contributor to heavy precipitation, these results for central Italy seem to slightly disagree with the atmospheric water budget outcomes concerning the role of surface evaporation. However, it is important to stress that moisture fluxes from the sea surface modify the thermodynamic profile of the air mass in the lower troposphere. This can have an indirect, complex and nonlinear impact on the downstream interaction between the low-level flow and the mountains (Apennines), thus modifying the intensity and amount of orographic precipitation (Stocchi and Davolio 2017), especially in areas characterized by convective instability. Moreover, it has been shown recently that evaporation may help supplying moisture to the AR (Dacre et al. 2019), and thus removing surface fluxes contribution could also affect AR-related precipitation. Therefore, a straightforward interpretation of these results can hardly be provided.

c. Discussion

The methodological procedure is worth an in-depth analysis in order to evaluate and discuss its possible uncertainties. First, the choice of the budget box position is crucial and requires special attention, since the box should intercept all and only the flow that supplies moisture to the downstream precipitation area. Therefore, since it is located where the low-level transport is intense, it also covers the area of the sea characterized by strong surface fluxes (i.e., evaporation). This also implies that the dimension of the box has to be adapted to the meteorological situation or to the specific event (Smith et al. 2010; Duffourg and Ducrocq 2013; Davolio et al. 2017). In the present study, a wider box has been used in the initial phase of the event, when the water vapor is conveyed towards northern Italy all over the western Mediterranean area. However, as the event evolves, the moisture transport becomes increasingly confined over the Tyrrhenian Sea, between Sardinia and the Italian coast, requiring an adaptation of the budget box. Note that this moisture transport pattern is shown by the IVT maps in Fig. 5d-f, and it is also confirmed by back-trajectories computation (see Section 4): the intensification of the AR progressively channels the trajectories within a narrow corridor. Thus, the budget box selected for the second phase of heavy precipitation over northern Italy largely overlaps the box used for the analysis over central Italy. Although the results would not change too much considering only one common box, this latter choice would not conform to the rationale behind the design of a suitable box. Both boxes in Figs. 7a,c are positioned in the area of intense moisture transport, but the smaller one is intended to evaluate only the contributions reaching the central Apennines.

The dimension of the box is also relevant since the mass balance terms are not normalized by a reference area and are expressed in kg s^{-1}. Therefore, since a larger section would allow higher values of the fluxes, including surface evaporation, it is very important to place the box correctly in order to account only for the mass transport of interest. On the other hand, the present case shows that regardless of the shape of the box, the meridional transport always exceeds the others, and the relative role of each contribution remains unchanged.

An accurate analysis of wind fields at different levels in the lower troposphere, possibly supported by trajectory computation, is critical for a correct selection of the box position and shape. It also allows to check that the flow is mainly horizontal and the loss across the top of the box is limited. However, this can be also checked by comparing the variation of total atmospheric water in the box (ΔIW in Eq. 1) against the sum of fluxes and evaporation. In our analysis, this residual term is always negligible, indicating that all the relevant contributions to the downstream precipitation are fairly evaluated.

6. Conclusions

The Vaia storm was a major severe weather event that affected Italy on 27–30 October 2018. It was characterized by extreme cumulated precipitation and fierce wind, causing floods, landslides, storm surges and waves. It was also responsible of high-impact on the environment, such as extensive damages to forests, and on the society, with interruption of traffic and electricity supply, other infrastructural damages and 16 casualties. The present study mainly focused on the heavy rainfall occurred in different parts of Italy and on the processes responsible to supply moisture to the precipitation systems. In particular, the presence of an AR transporting large amounts of moisture from the tropical Atlantic, through Africa, to the Mediterranean basin has been demonstrated. The same diagnostics and the same parameter thresholds, widely adopted for the US Pacific coast to detect ARs, proved to be suitable also for the Mediterranean, despite the AR moving mainly over the African continent. The AR was about 3000 km long and confined in the lower troposphere, below 3000 m all along its path. Over the Mediterranean, due to the high moisture content and intense winds (low-level jet), it reached its maximum intensity, with an IVT slightly exceeding 1500 kg m^{-1} s^{-1}.

A detailed diagnostic, based on the water budget computation within atmospheric boxes placed over the Mediterranean suitably located upstream of the precipitation areas, has revealed the primary contribution of the AR to the heavy precipitation water supply. Although the possible presence of

ARs over the Mediterranean was already suggested in recent studies (Buzzi et al. 2014; Krichak et al. 2015), to our knowledge this is the first time that the role of an AR is quantitatively evaluated in this area. In fact, the adopted methodology, that integrates in space and time the atmospheric water fluxes obtained by numerical simulations, allowed to disentangle the local contribution of moisture, that is evaporation from the sea, from the transport from remote sources, quantifying their relative importance. During this storm, the contribution of evaporation from the sea turned out to be much less important than the moisture transport, which came mainly from the southern Mediterranean area, with a contribution from the Atlantic during the first day, until the evening of 27 October. In particular, the moisture transport from the south, associated with the AR, was critical for feeding the precipitation in central Italy, which is more directly exposed to moisture advection from the south. However, the AR contribution turned out to be a key factor also for the heavy precipitation over northern Italy, although this important role is limited to the second intense phase of the event, occurred on 29 October.

The sensitivity experiments confirmed these findings and the first one incidentally showed that the AR had some impacts also on the explosive deepening of the Mediterranean cyclone. A close link between ARs and extratropical cyclones has been recently proposed, since ARs seem to provide favorable conditions for explosive cyclogenesis (Ferreira et al. 2016; Eiras-Barca et al. 2018). The investigation of this aspect is out of the scope of the present paper, but it is already planned as a follow up. Finally, it is worth mentioning that the event shared many interesting characteristics (synoptic evolution, rainfall intensity, winds and surge) with the 1966 event, known as the “century” flood in Italy (Malguzzi et al. 2006; De Zolt et al. 2006). This suggests that a climatological investigation, in order to evaluate the presence and importance of ARs in the Mediterranean in correspondence with heavy precipitation events, should be the next step of this research topic.

A major “take away” lesson learned during this study is that ARs do influence the meteorology of the Mediterranean, particularly the precipitation structure of certain intense precipitation events. However, their role is not easy to detect due to many superimposed factors and processes that influence the meteorology of the basin, especially the complex orography, the sea-land distribution and the simultaneous action of Atlantic, northern European and tropical air masses. Thus, an unambiguous detection of an AR and of its effects in the area needs particular care, perhaps more than in other areas of the world where ARs are associated with more clear-cut structures.

Acknowledgments. This work is a contribution to the HyMeX international program. The authors are grateful to the National Department of Civil Protection for having grant the access to Dewetra platform and raingauge data, in the framework of the contract “Intesa Operativa con CNR- ISAC”.

REFERENCES

Anquetin, S., E. Yates, V. Ducrocq, S. Samouillan, K. Chancibault, S. Davolio, C. Accadia, M. Casaioli, S. Mariani, G. Ficca, B. Gozzini, F. Pasi, M. Pasqui, M. Garcia, M. Martorell, R. Romero, and P. Chessa, 2005: The 8 and 9 September 2002 flash flood event in France: A model intercomparison. *Nat. Hazard Earth Syst. Sci.*, **5**, 741-754, https://doi.org/10.5194/nhess-5-741-2005.

ARPAV, 2018: 27-30 ottobre 2018. Maltempo in Veneto: Pioggia e vento eccezionali. [available at https://www.arpa.veneto.it/arpav/pagine-generiche/emergenze-ambientali/storico-emergenze-ambientale/27-30-ottobre-2018.-maltempo-in-veneto-pioggia-e-vento-eccezionali, in Italian]

Benedict, I., K. Odemark, T. Nipen, and R. Moore, 2019: Large-scale flow patterns associated with extreme precipitation and atmospheric rivers over Norway. *Mon. Wea. Rev.*, **147**, 1415-1428, https://doi.org/10.1175/MWR-D-18-0362.1.

Bertò, A., A. Buzzi, and D. Zardi, 2004: Back-tracking water vapour contributing to a precipitation event over Trentino: A case study. *Meteor. Z.*, **13(3)**, 189-200, https://doi.org/10.1127/0941-2948/2004/0013-0189.

Bougeault, P., P. Binder, A. Buzzi, R. Dirks, J. Kuettner, R. B. Smith, R. Steinacker, and H. Volkert, 2001: The MAP special observing period. *Bull. Amer. Meteor. Soc.*, **82**, 433–462, https://doi.org/10.1175/1520-0477(2001)082<0433:TMSOP>2.3.CO;2.

Browning, K., 2018: Atmospheric rivers in the U.K. *Bull. Amer. Meteor. Soc.*, **99**, 1108–1109, https://doi.org/10.1175/BAMS-D-17-0291.1.

Buzzi, A., M. D'Isidoro, and S. Davolio, 2003: A case study of an orographic cyclone south of the Alps during the MAP SOP. *Quart. J. Roy. Meteor. Soc.*, **129**, 1795–1818, https://doi.org/10.1256/qj.02.112.

Buzzi, A., S. Davolio, P. Malguzzi, O. Drofa, and D. Mastrangelo, 2014: Heavy rainfall episodes over Liguria of autumn 2011: Numerical forecasting experiments. *Nat. Hazards Earth Syst. Sci.*, **14**, 1325–1340, https://doi.org/10.5194/nhess-14-1325-2014.

Cavaleri, L., M. Bajo, F. Barbariol, M. Bastianini, A. Benetazzo, L. Bertotti, J. Chiggiato, S. Davolio, C. Ferrarin, L. Magnusson, A. Papa, P. Pezzutto, A. Pomaro, and G. Umgiesser, 2019: The October 29, 2018 storm in Northern Italy - An exceptional event and its modeling. *Progr. Oceanography*, **178**, 102178, https://doi.org/10.1016/j.pocean.2019.102178.

Dacre, H. F., O. Martínez-Alvarado, and C. O. Mbengue, 2019: Linking atmospheric rivers and warm conveyor belt airflows. *J. Hydrometeor.*, **20**, 1183–1196, https://doi.org/10.1175/JHM-D-18-0175.1.

Dacre, H. F., P. A. Clark, O. Martinez-Alvarado, M. A. Stringer, and D. A. Lavers, 2015: How do atmospheric rivers form? *Bull. Amer. Meteor. Soc.*, **96**, 1243-1255, https://doi.org/10.1175/BAMS-D-14-00031.1.

Davolio, S., M. M. Miglietta, T. Diomede, C. Marsigli, and A. Montani, 2013: A flood episode in Northern Italy: Multi-model and single-model mesoscale meteorological ensembles for hydrological predictions *Hydrol. Earth Syst. Sci.*, **17**, 1-14, https://doi.org/10.5194/hess-17-2107-2013.

Davolio, S., R. Henin, P. Stocchi and A. Buzzi, 2017: Bora wind and heavy persistent precipitation: atmospheric water balance and role of air-sea fluxes over the Adriatic Sea. *Quart. J. Roy. Meteor. Soc.*, **143**, 1165-1177, https://doi.org/10.1002/qj.3002.

De Zolt, S., P. Lionello, A. Nuhu, and A. Tomasin, 2006: The disastrous storm of 4 November 1966 on Italy. *Nat. Hazards Earth Syst. Sci.*, **6**, 861–879, https://doi.org/10.5194/nhess-6-861-2006.

Drobinski, P., V. Ducrocq, P. Alpert, E. Anagnostou, K. Béranger, M. Borga, I. Braud, A. Chanzy, S. Davolio, G. Delrieu, C. Estournel, N. Filali Boubrahmi, J. Font, V. Grubišić, S. Gualdi, V. Homar, B. Ivančan-Picek, C. Kottmeier, V. Kotroni, K. Lagouvardos, P. Lionello, M. C. Llasat, W. Ludwig, C. Lutoff, A. Mariotti, E. Richard, R. Romero, R. Rotunno, O. Roussot, I. Ruin, S. Somot, I. Taupier-Letage, J. Tintore, R. Uijlenhoet, and H. Wernli, 2014: HyMeX, a 10-year multidisciplinary program on the Mediterranean water cycle. *Bull. Amer. Meteor. Soc.*, **95**, 1063-1082, https://doi.org/10.1175/BAMS-D-12-00242.1.

Drofa, O., and P. Malguzzi, 2004: Parameterization of microphysical processes in a non hydrostatic prediction model. *Proc. 14th Int. Conf. on Clouds and Precipitation (ICCP)*, Bologna, 19–23 July 2004, 1297–3000.

Duffourg, F., and V. Ducrocq, 2011: Origin of the moisture feeding the heavy precipitating systems over southeastern France. *Nat. Hazards Earth Syst. Sci.*, **11**, 1163–1178, https://doi.org/10.5194/nhess-11-1163-2011.

Duffourg, F., and V. Ducrocq, 2013: Assessment of the water supply to Mediterranean heavy precipitation: A method based on finely designed water budgets. *Atmos. Sci. Lett.*, **14**, 133–138, https://doi.org/10.1002/asl2.429.

Eiras-Barca, J., A. Ramos, J. Pinto, R. Trigo, M. Liberato, and G. Miguez-Macho, 2018: The concurrence of atmospheric rivers and explosive cyclogenesis in the North Atlantic and North Pacific basins. *Earth Syst. Dyn.*, **9**, 91-102, https://doi.org/10.5194/esd-9-91-2018.

Ferreira, J. A., M. Liberato, and A. M. Ramos, 2016: On the relationship between atmospheric water vapour transport and extra-tropical cyclones development. *Phys. Chem. Earth, Parts A/B/C*, **94**, 56-65, https://doi.org/10.1016/j.pce.2016.01.001.

Gimeno, L., R. Nieto, M. Vàsquez, and D. A. Lavers, 2014: Atmospheric rivers: A mini-review. *Front. Earth Sci*., **2**, https://doi.org/10.3389/feart.2014.00002.

Grazzini, F., 2007: Predictability of a large-scale flow conducive to extreme precipitation over the western Alps. *Meteor. Atmos. Phys*., **95**, 123–138, https://doi.org/10.1007/s00703-006-0205-8.

Grazzini, F., C. G. Craig, C. Keil, G. Antolini, and V. Pavan, 2019: Extreme precipitation events over northern Italy. Part I: A systematic classification with machine-learning techniques. *Quart. J. Roy. Meteor. Soc*., **146**, 69-85, https://doi.org/10.1002/qj.3635.

Hubbard, M. E., and N. Nikiforakis, 2003: A three-dimensional adaptive, Godunov type model for global atmospheric flows I: Tracer advection on fixed grids. *Mon. Wea. Rev.,* **131**, 1848-1864, https://doi.org/10.1175//2568.1.

Kain, J. S., 2004: The Kain–Fritsch convective parameterization: An update. *J. Appl. Meteor*., **43**, 170–181, https://doi.org/10.1175/1520-0450(2004)043<0170:TKCPAU>2.0.CO;2.

Khodayar, S., N. Kalthoff, and C. Kottmeier, 2018: Atmospheric conditions associated with heavy precipitation events in comparison to seasonal means in the western Mediterranean region. *Clim. Dyn*., **51(3)**, 951-967, https://doi.org/10.1007/s00382-016-3058-y.

Knippertz, P., and H. Wernli, 2010: A lagrangian climatology of tropical moisture exports to the northern hemispheric extratropics. *J. Climate*, **23**, 987–1003, https://doi.org/10.1175/2009JCLI3333.1.

Krichak, S. O., J. Barkan, J. S. Breitgand, S. Gualdi, and S. B. Feldstein, 2015: The role of the export of tropical moisture into midlatitudes for extreme precipitation events in the Mediterranean region. *Theor. Appl. Climatol*., **121**, 499–515, https://doi.org/10.1007/s00704-014-1244-6.

Krichak, S. O., S. B. Feldstein, P. Alpert, S. Gualdi, E. Scoccimarro, and J.-I. Yano, 2016: Discussing the role of tropical and subtropical moisture sources in cold season extreme precipitation events in the Mediterranean region from a climate change perspective. *Nat. Hazards Earth Syst. Sci.*, **16**, 269-285, https://doi.org/10.5194/nhess-16-269-2016.

Jansa, A., P. Alpert, P. Arbogast, A. Buzzi, B. Ivančan-Picek, V. Kotroni, M. C. Llasat, C. Ramis, E. Richard, R. Romero, and A. Speranza, 2014: MEDEX: A general overview. *Nat. Hazards Earth Syst. Sci.*, **14**, 1965–1984, https://doi.org/10.5194/nhess-14-1965-2014.

Lavers, D. A., and G. Villarini, 2013: The nexus between atmospheric rivers and extreme precipitation across Europe. *Geophys. Res. Lett.*, **40**, 3259–3264, https://doi.org/10.1002/grl.50636.

Lavers, D. A., R. P. Allan, E. F. Wood, G. Villarini, D. J. Brayshaw, and A. J. Wade, 2011: Winter floods in Britain are connected to atmospheric rivers. *Geophys. Res. Lett.*, **38**, L23803, https://doi.org/10.1029/2011GL049783.

Liberato, M. L., A. M. Ramos, R. M. Trigo, I. F. Trigo, A. M. Durán-Quesada, R. Nieto, and L. Gimeno, 2012: Moisture sources and large-scale dynamics associated with a flash flood event. In: *Lagrangian Modeling of the Atmosphere*, J. Lin, D. Brunner, C. Gerbig, A. Stohl, A. Luhar, P. Webley, Eds., *Geophys. Monogr.*, **200**, Amer. Geophys. Union, 111–126, https://doi.org/10.1029/2012GM001244.

Magnusson, L., and L. Cavaleri, 2019: Predicting multiple weather hazards over Italy. *ECMWF Newsletter*, **158**, 2-3 [available at https://www.ecmwf.int/sites/default/files/elibrary/2019/18821-newsletter-no-158-winter-201819.pdf].

Malguzzi, P., G. Grossi, A. Buzzi, R. Ranzi, and R. Buizza, 2006: The 1966 “century” flood in Italy: A meteorological and hydrological revisitation. *J. Geophys. Res.*, **111**, D24106, https://doi.org/10.1029/2006JD007111.

Mariani, S., M. Casaioli, C. Accadia, M. C. Llasat, F.Pasi, S. Davolio, M. Elementi, G. Ficca, and R. Romero, 2005: A limited area model intercomparison on the "Montserrat-2000" flash-flood event using statistical and deterministic methods. *Nat. Hazard Earth Syst. Sci.,* **5**, 565-581, https://doi.org/10.5194/nhess-5-565-2005.

Martius, O., C. Schwierz, and H. C. Davies, 2008: Far-upstream precursors of heavy precipitation events in the Alpine south-side. *Quart. J. Roy. Meteor. Soc.*, **134**, 417-428, https://doi.org/10.1002/qj.229.

Massacand, A. C., H. Wernli, and H. C. Davies, 1998: Heavy precipitation on the Alpine southside: An upper-level precursor. *Geophys. Res. Lett.*, **25(9)**, 1435–1438, https://doi.org/10.1029/98GL50869.

Miglietta, M. M., and R. Rotunno, 2006: Further results on moist nearly neutral flow over a ridge. *J. Atmos. Sci.*, **63**, 2881–2897, https://doi.org/10.1175/JAS3793.1.

Morcrette, J.-J., H. W. Barker, J. N. S. Cole, M. J. Iacono, and R. Pincus, 2008: Impact of a new radiation package, McRad, in the ECMWF Integrated Forecasting System. *Mon. Wea. Rev.*, **136**, 4773–4798, https://doi.org/10.1175/2008MWR2363.1.

Motta, R., D. Ascoli, P. Corona, M. Marchetti, and G. Vacchiano, 2018: Selvicoltura e schianti da vento. Il caso della "tempesta Vaia". *Forest@*, **15**, 94-98, https://doi.org/10.3832/efor2990-015 (in Italian).

Neiman, P. J., L. J. Schick, F. M. Ralph, M. Hughes, and G. A. Wick, 2011: Flooding in western Washington: The connection to atmospheric rivers. *J. Hydrometeor.*, **12**, 1337-1358, https://doi.org/10.1175/2011JHM1358.1.

Pinto, J. G., S. Ulbrich, A. Parodi, R. Rudari, G. Boni, and U. Ulbrich, 2013: Identification and ranking of extraordinary rainfall events over Northwest Italy: The role of Atlantic moisture. *J. Geophys. Res.*, **118**, 2085–2097, https://doi.org/10.1002/jgrd.50179.

Ralph, F. M., and M. D. Dettinger, 2011: Storms, floods, and the science of atmospheric rivers. *EoS*, **92**, 265-266, https://doi.org/10.1029/2011EO320001.

Ralph, F. M., P. J. Neiman, and G. A. Wick, 2004: Satellite and CALJET aircraft observations of atmospheric rivers over the eastern North Pacific Ocean during the winter of 1997/98. *Mon. Wea. Rev.*, **132**, 1721-1745, https://doi.org/10.1175/1520-0493(2004)132<1721:SACAOO>2.0.CO;2.

Ralph, F. M., M. D. Dettinger, M. M. Cairns, T. J. Galarneau, and J. Eylander, 2018: Defining "atmospheric river": How the Glossary of Meteorology helped resolve a debate. *Bull. Amer. Meteor. Soc.*, **99**, 837–839, https://doi.org/10.1175/BAMS-D-17-0157.1.

Ralph, F. M., J. J. Rutz, J. M. Cordeira, M. Dettinger, M. Anderson, D. Reynolds, L. I. Schick, and C. Smallcomb, 2019: A scale to characterize the strength and impacts of atmospheric rivers. *Bull. Amer. Meteor. Soc.*, **100**, 269-290, https://doi.org/10.1175/BAMS-D-18-0023.1.

Ramos, A. M., R. M. Trigo, M. L. R. Liberato, and R. Tome, 2015: Daily precipitation extreme events in the Iberian Peninsula and its association with atmospheric rivers. *J. Hydrometeor.*, **16**, 579–597, https://doi.org/10.1175/JHM-D-14-0103.1.

Reale, O., K. Feudale, and B. Turato, 2001: Evaporative moisture sources during a sequence of floods in the Mediterranean region. *Geophys. Res. Lett.*, **28(10)**, 2085-2088, https://doi.org/10.1029/2000GL012379.

Ritter, B., and J. F. Geleyn, 1992: A comprehensive radiation scheme for numerical weather prediction models with potential applications in climate simulations. *Mon. Wea. Rev.*, **120**, 303–325, https://doi.org/10.1175/1520-0493(1992)120<0303:ACRSFN>2.0.CO;2.

Rolph, G., A. Stein, and B. Stunder, 2017: Real-time Environmental Applications and Display sYstem: READY. *Environ. Model. Softw.*, **95**, 210-228, https://doi.org/10.1016/j.envsoft.2017.06.025.

Rudari, R., D. Entekhabi, and G. Roth, 2005: Large-scale atmospheric patterns associated with mesoscale features leading to extreme precipitation events in Northwestern Italy. *Adv. Water Res.*, **28**, 601-614, https://doi.org/10.1016/j.advwatres.2004.10.017.

Rutz, J. J., W. J. Steenburgh, and F. M. Ralph, 2014: Climatological characteristics of atmospheric rivers and their inland penetration over the western United States. *Mon. Wea. Rev.*, **142**, 905-921, https://doi.org/10.1175/MWR-D-13-00168.1.

Sanders, F., and J. R. Gyakum, 1980: Synoptic-dynamic climatology of the "bomb". *Mon. Wea. Rev.*, **108**, 1589-1606, https://doi.org/10.1175/1520-0493(1980)108<1589:SDCOT>2.0.CO;2.

Smith, B. L., S. E. Yuter, P. J. Neiman, D. E. Kingsmill, 2010: Water vapor fluxes and orographic precipitation over northern California associated with a landfalling atmospheric river. *Mon. Wea. Rev.*, **138**, 74-100, https://doi.org/10.1175/2009MWR2939.1.

Sodemann, H., and A. Stohl, 2013: Moisture origin and meridional transport in atmospheric rivers and their association with multiple cyclones. *Mon. Wea. Rev.*, **141**, 2850–2868, https://doi.org/10.1175/MWR-D-12-00256.1.

Stein, A. F., R. R. Draxler, G. D. Rolph, B. J. B. Stunder, M. D. Cohen, and F. Ngan, 2015: NOAA's HYSPLIT atmospheric transport and dispersion modeling system. *Bull. Amer. Meteor. Soc.*, **96**, 2059-2077, https://doi.org/10.1175/BAMS-D-14-00110.1.

Stocchi, P., and S. Davolio, 2017: Intense air-sea exchanges and heavy orographic precipitation over Italy: the role of the Adriatic Sea surface temperature uncertainty. *Atmos. Res.*, **196**, 62-82, https://doi.org/10.1016/j.atmosres.2017.06.004.

Turato, B., O. Reale, and F. Siccardi, 2004: Water vapor sources of the October 2000 Piedmont flood. *J. Hydrometeor.*, **5**, 693–712, https://doi.org/10.1175/1525-7541(2004)005<0693:WVSOTO>2.0.CO;2.

Wimmers, A. J., and C. S. Velden, 2011: Seamless advective blending of total precipitable water retrievals from polar-orbiting satellites. *J. Appl. Meteor. Climatol.*, **50**, 1024-1036. doi: http://dx.doi.org/10.1175/2010JAMC2589.1

Winschall, A., S. Pfahl, H. Sodemann, and H. Wernli, 2012: Impact of North Atlantic evaporation hot spots on southern Alpine heavy precipitation events. *Quart. J. Roy. Meteor. Soc.*, **138**, 1245–1258, https://doi.org/10.1002/qj.987.

Winschall, A., H. Sodemann, S. Pfahl, and H. Wernli, 2014: How important is intensified evaporation for Mediterranean precipitation extremes? *J. Geophys. Res.*, **119**, 5240-5256, https://doi.org/10.1002/2013JD021175.

Zampieri, M., P. Malguzzi, and A. Buzzi, 2005: Sensitivity of quantitative precipitation forecasts to boundary layer parameterization: A flash flood case study in the western Mediterranean. *Nat. Hazards Earth Syst. Sci*., **5**, 603–612, https://doi.org/10.5194/nhess-5-603-2005.

Zhu, Y., and R. E. Newell, 1998: A proposed algorithm for moisture fluxes from atmospheric rivers. *Mon. Wea. Rev*., **126**, 725–735, https://doi.org/10.1175/1520-0493(1998)126<0725:APAFMF>2.0.CO;2.

Tables

TABLE 1. Contribution relative to the total water mass entering the budget box, due to the transport across the box sides and to evaporation, during the two phases of precipitation over the northern Italy area. Computation is based on the large box in Fig. 3 for the first phase, and on the box in Fig. 7a for the second phase.

Budget term	Contribution First phase %	Contribution Second phase %
South Section	55	66
West Section	24	13
East Section	0	9
Evaporation	21	12

TABLE 2. Same as Table 1, but for the three phases of precipitation over the central Italy area (computation is made considering the box in Fig. 7c).

Budget term	Contribution First phase %	Contribution Second phase %	Contribution Third phase %
South Section	57	57	47
West Section	24	19	19
East Section	8	12	15
Evaporation	11	12	19

TABLE 3. Summary of the numerical sensitivity experiments and their acronyms.

Experiment acronym	Experiment details
REF	Control simulation on the smallest domain (Fig.3)
SBND	Moisture entering the southern boundary reduced by 75%
NOFL	Surface latent heat fluxes switched off over the Mediterranean Sea during the whole simulation, since 12 UTC, 26 Oct.
NOFL48	As NOFL, but fluxes are switched off only since 12 UTC, 28 Oct.

Figure Caption List

FIG. 1. Global Forecast System (GFS) analyses of 500 hPa geopotential height, 500-1000 hPa thickness and mean sea level pressure at 0000 UTC on (a) 27, (b) 28 and (c) 29 Oct. 2018. (d) UK Met Office analysis of mean sea level pressure and fronts at 1800 UTC, 29 Oct. 2018 in correspondence of the maximum intensity of the Mediterranean cyclone.

FIG. 2. Accumulated precipitation (interpolation of the Italian raingauge network): (a) 48-h rainfall during 27 and 28 Oct. 2018, (b) 24-h rainfall on 29 Oct. 2018. Rainfall maps are provided by the National Civil Protection Department through the Dewetra platform.

FIG. 3. BOLAM integration domain and orography (grey shading corresponds to 500, 1000 and 2000 m). The inner dashed box indicates the integration domain employed for the sensitivity experiment described in Section 5b. The inner solid box indicates the atmospheric volume for the water budget computation.

FIG. 4. 72-h accumulated precipitation (0000 UTC 27 Oct. – 0000 UTC 30 Oct., 2018) as simulated by BOLAM. The area is a small portion of the entire integration domain shown in Fig.3. Location of Udine radiosounding (NE Italy) is indicated with a star.

FIG. 5. Simulated Integrated Water Vapor (mm, color shading) and geopotential height at 500 hPa (m, contour) at 1200 UTC on (a) 27, (b) 28 and (c) 29 Oct. 2018. Simulated Integrated Vapor Transport (kg m^{-1} s^{-1}, color shading and arrows) and mean sea level pressure (hPa, contour) at 1200 UTC on (d) 27, (e) 28 and (f) 29 Oct. 2018. Morphed Integrated Microwave Total Precipitable Water (MIMIC-TPW) at 1200 UTC on (g) 27, (h) 28, and (i) 29 Oct. 2018 (ftp://ftp.ssec.wisc.edu/pub/mtpw2). The inner solid box indicates the atmospheric volume for the water budget computation (also shown in Fig. 3).

FIG. 6. (a) Area identified as AR at 1800 UTC, 28 Oct. 2018, (blue shading) characterized by IWV > 2 cm and IVT > 250 kg m^{-1} s^{-1}, and geopotential height at 700 hPa (m, contour). The dashed line indicates the location of the cross section shown in Fig. 6b. (b) Vertical cross section of water vapor flux (g m^{-2} s^{-1}, color shading) and normal wind speed component (m s^{-1}, contour lines every 5 m s^{-1}) at 1800 UTC, 28 Oct. 2018.

FIG. 7. Small solid boxes indicate the area used to compute hourly averaged precipitation over (a) northern Italy and (c) central Italy. Large dashed boxes are used for the atmospheric water budget computation and analysis concerning the precipitation over (a) north and (c) central Italy. Grey shading for the orography in (a) and (c) corresponds to 500, 1000 and 2000 m. Area-averaged hourly precipitation over (b) the northern Italy area and (d) the central Italy area. Gray shading indicates the analyzed phases of precipitation.

FIG. 8. Evolution of the atmospheric water budget associated with the precipitation over northern Italy, computed (a) in the large box over the Mediterranean shown in Fig. 3 and (b) in the box shown in Fig. 7a. Positive values indicate incoming fluxes. Solid lines indicate fluxes across the four lateral sides of the box. The two shaded bars at the top indicate the time window for the integration of the lateral fluxes (blue) and evaporation (red).

FIG. 9. As in Fig. 8 but for precipitation over central Italy within the box shown in Fig. 7c.

FIG. 10. Area-averaged hourly precipitation over (a) the northern and (b) the central Italy area. Green histograms for the reference simulations, black solid line for the sensitivity experiments (SBND) with reduced moisture across the southern boundary.

Fig. 11. Integrated Vapor Transport (kg m^{-1} s^{-1}, color shading and arrows) at 0000 UTC, 29 Oct. 2018 for (a) the reference simulation (REF) and (b) the sensitivity experiments (SBND) with reduced moisture across the southern boundary. The two boxes (shown also in Figs. 7a,c) used to compute the atmospheric water budget concerning rainfall over northern Italy (larger box) and central Italy (smaller box) are also plotted.

FIG. 12. Area-averaged hourly precipitation over the central Italy area. Reference simulation (REF, green histograms), and the two sensitivity experiments without evaporation from the sea since the beginning (NOFL, black solid line) and after 48 h of simulation (NOFL48, red solid line).

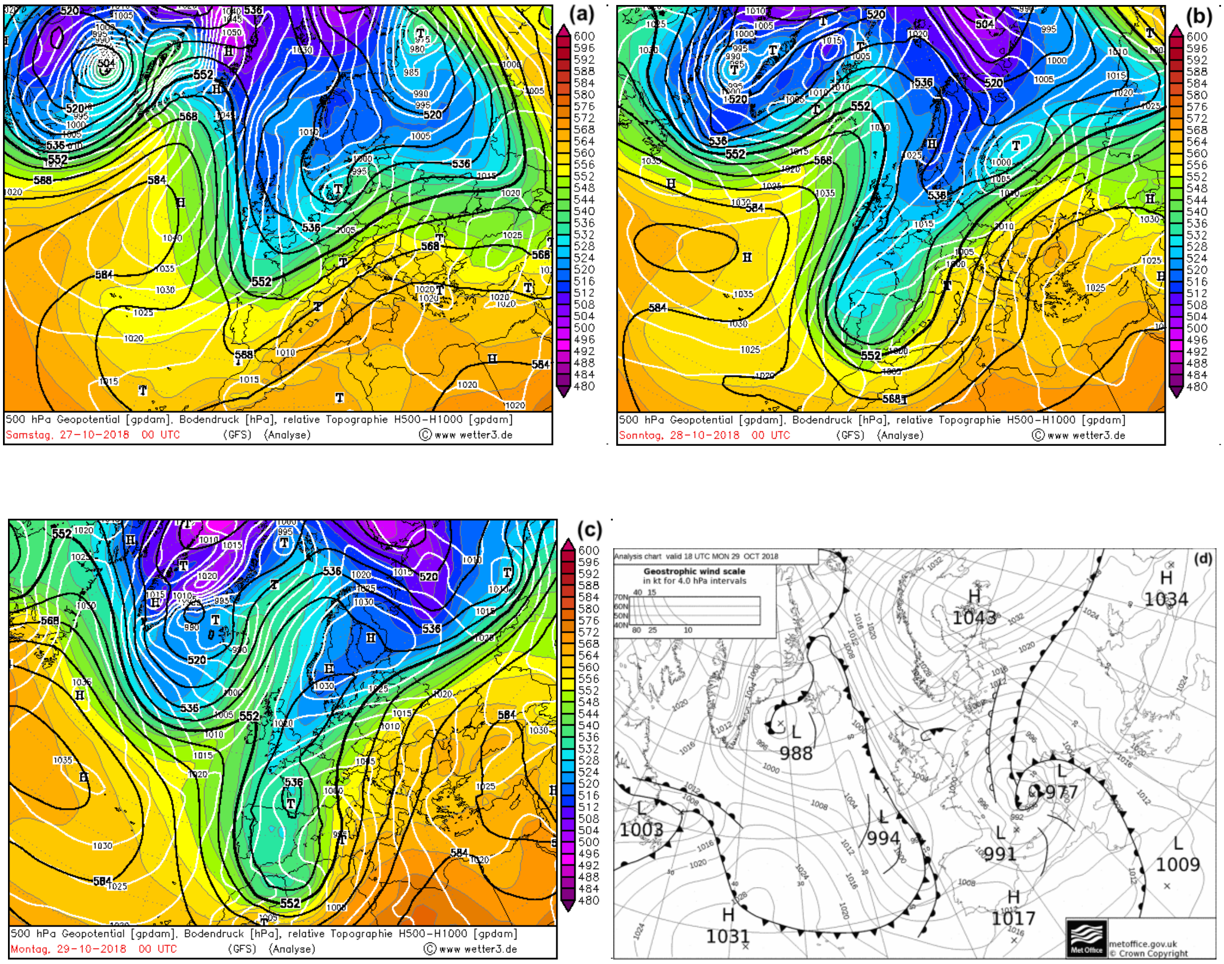

FIG. 1. Global Forecast System (GFS) analyses of 500 hPa geopotential height, 500-1000 hPa thickness and mean sea level pressure at 0000 UTC on (a) 27, (b) 28 and (c) 29 Oct. 2018. (d) UK Met Office analysis of mean sea level pressure and fronts at 1800 UTC, 29 Oct. 2018 in correspondence of the maximum intensity of the Mediterranean cyclone.

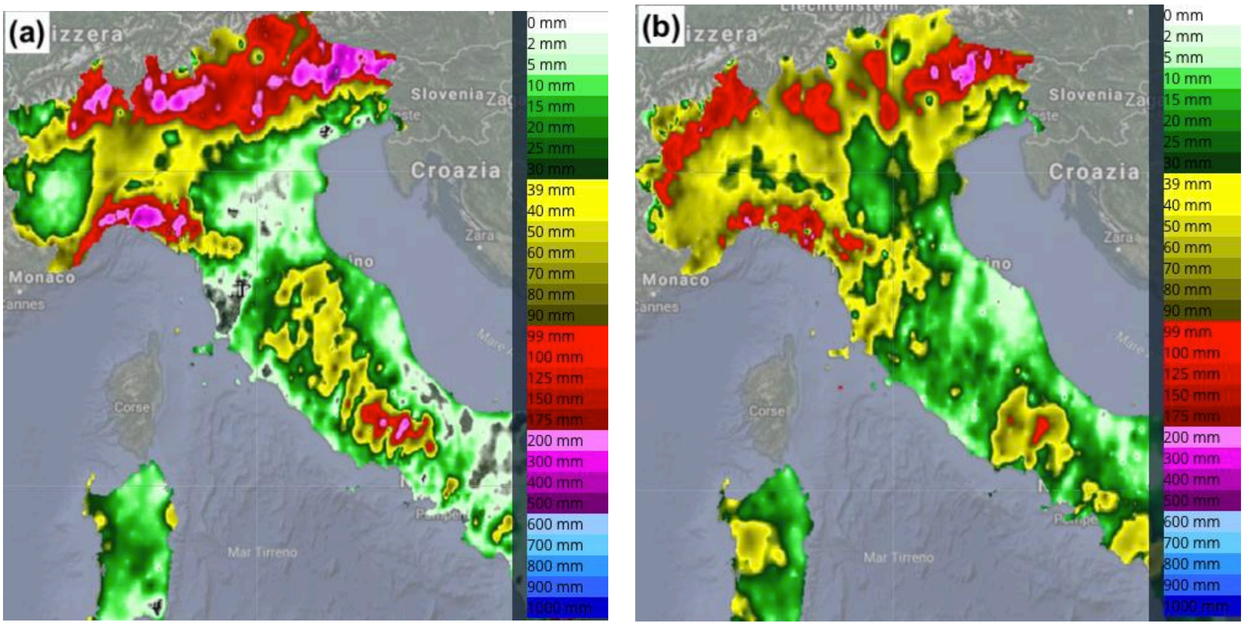

FIG. 2. Accumulated precipitation (interpolation of the Italian raingauge network): (a) 48-h rainfall during 27 and 28 Oct. 2018, (b) 24-h rainfall on 29 Oct. 2018. Rainfall maps are provided by the National Civil Protection Department through the Dewetra platform.

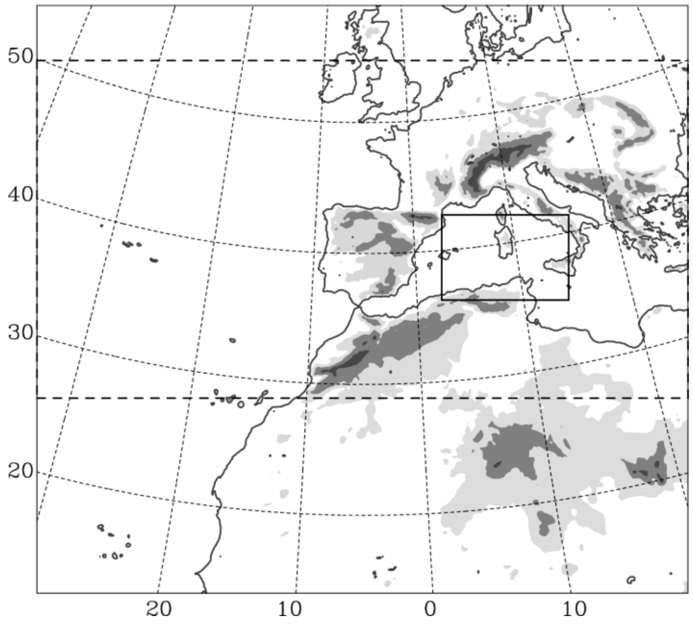

FIG. 3. BOLAM integration domain and orography (grey shading corresponds to 500, 1000 and 2000 m). The inner dashed box indicates the integration domain employed for the sensitivity experiment described in Section 5b. The inner solid box indicates the atmospheric volume for the water budget computation.

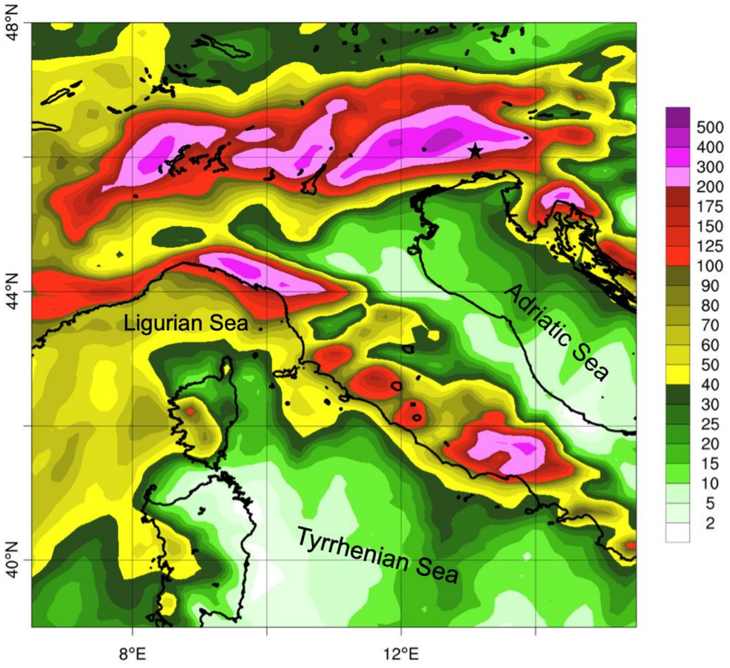

FIG. 4. 72-h accumulated precipitation (0000 UTC 27 Oct. – 0000 UTC 30 Oct., 2018) as simulated by BOLAM. The area is a small portion of the entire integration domain shown in Fig.3. Location of Udine radiosounding (NE Italy) is indicated with a star.

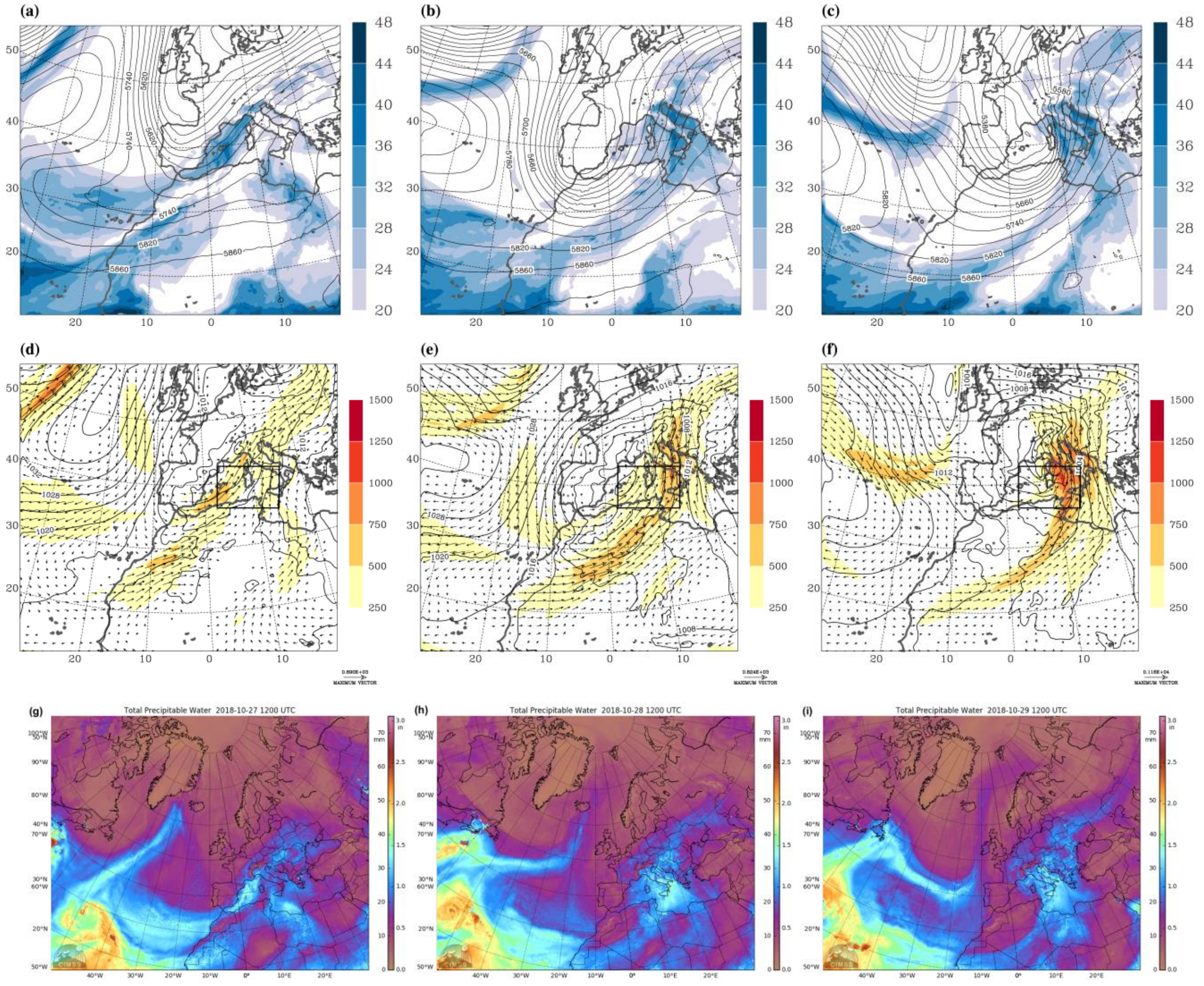

FIG. 5. Simulated Integrated Water Vapor (mm, color shading) and geopotential height at 500 hPa (m, contour) at 1200 UTC on (a) 27, (b) 28 and (c) 29 Oct. 2018. Simulated Integrated Vapor Transport (kg m^{-1} s^{-1}, color shading and arrows) and mean sea level pressure (hPa, contour) at 1200 UTC on (d) 27, (e) 28 and (f) 29 Oct. 2018. Morphed Integrated Microwave Total Precipitable Water (MIMIC-TPW) at 1200 UTC on (g) 27, (h) 28, and (i) 29 Oct. 2018 (ftp://ftp.ssec.wisc.edu/pub/mtpw2). The inner solid box indicates the atmospheric volume for the water budget computation (also shown in Fig. 3).

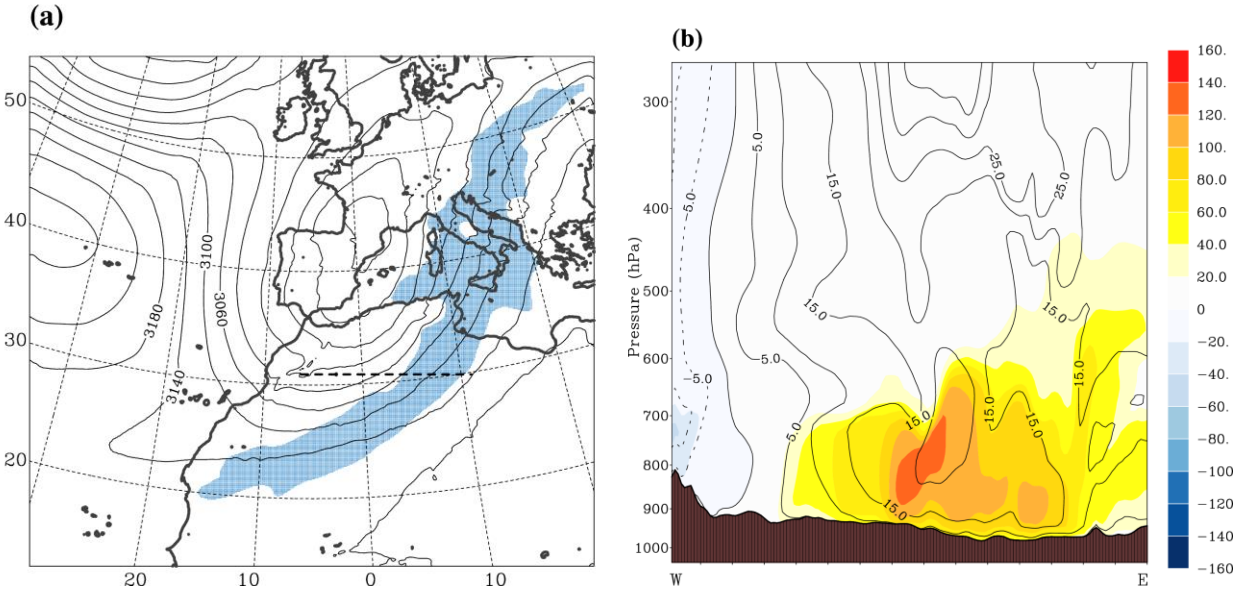

FIG. 6. (a) Area identified as AR at 1800 UTC, 28 Oct. 2018, (blue shading) characterized by IWV > 2 cm and IVT > 250 kg m^{-1} s^{-1}, and geopotential height at 700 hPa (m, contour). The dashed line indicates the location of the cross section shown in Fig. 6b. (b) Vertical cross section of water vapor flux (g m^{-2} s^{-1}, color shading) and normal wind speed component (m s^{-1}, contour lines every 5 m s^{-1}) at 1800 UTC, 28 Oct. 2018.

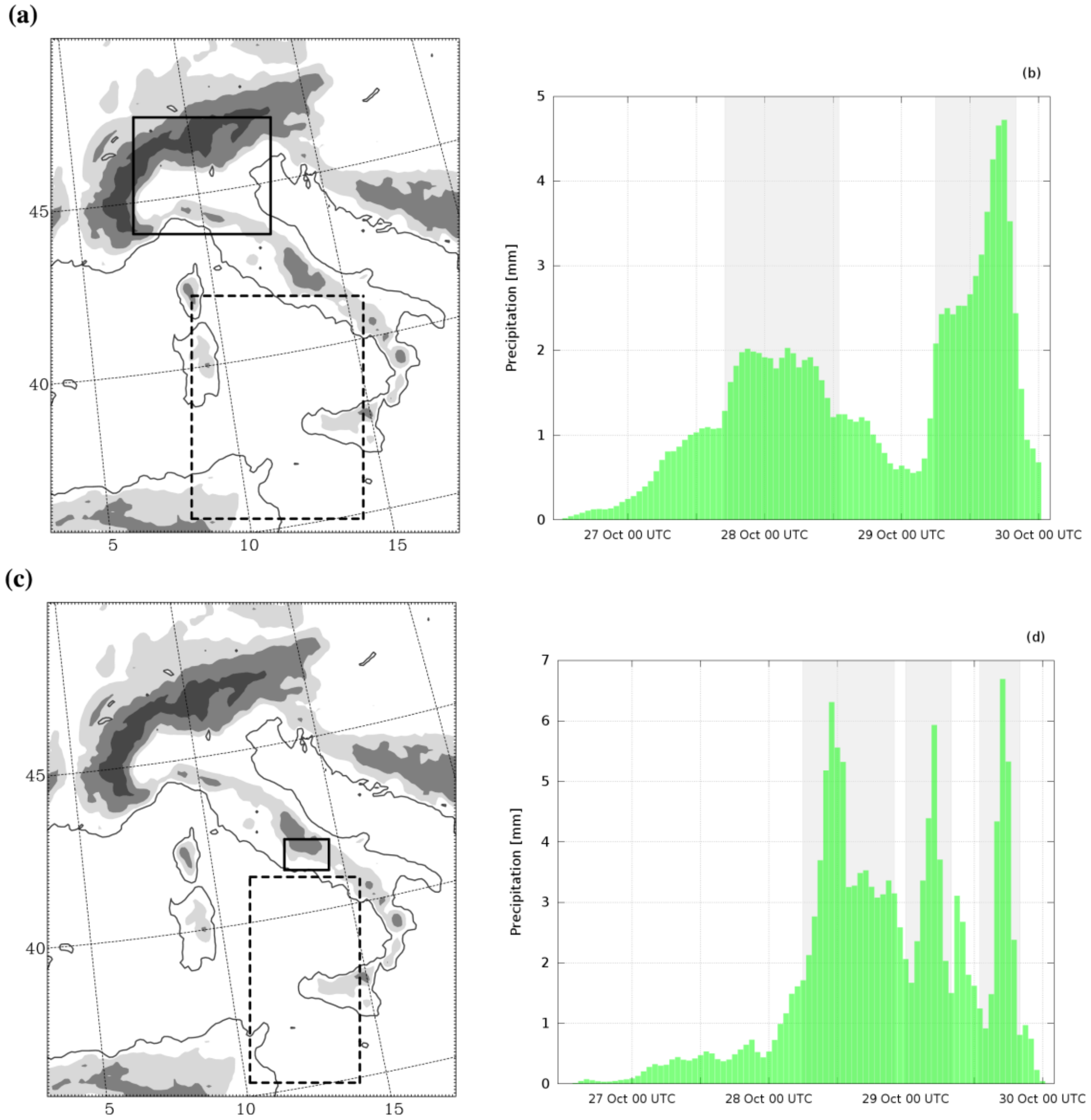

FIG. 7. Small solid boxes indicate the area used to compute hourly averaged precipitation over (a) northern Italy and (c) central Italy. Large dashed boxes are used for the atmospheric water budget computation and analysis concerning the precipitation over (a) north and (c) central Italy. Grey shading for the orography in (a) and (c) corresponds to 500, 1000 and 2000 m. Area-averaged hourly precipitation over (b) the northern Italy area and (d) the central Italy area. Gray shading indicates the analyzed phases of precipitation.

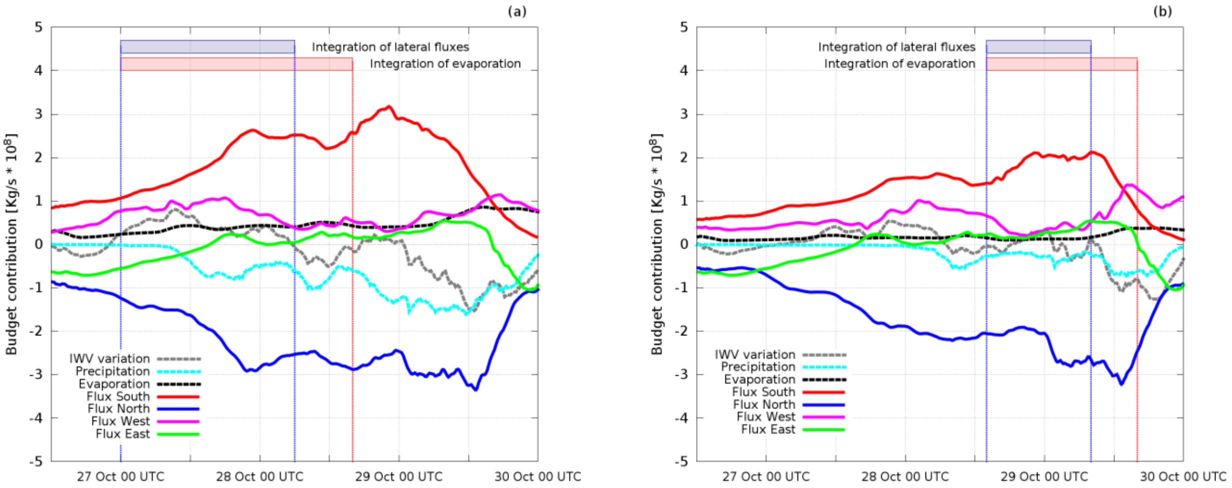

FIG. 8. Evolution of the atmospheric water budget associated with the precipitation over northern Italy, computed (a) in the large box over the Mediterranean shown in Fig. 3 and (b) in the box shown in Fig. 7a. Positive values indicate incoming fluxes. Solid lines indicate fluxes across the four lateral sides of the box. The two shaded bars at the top indicate the time window for the integration of the lateral fluxes (blue) and evaporation (red).

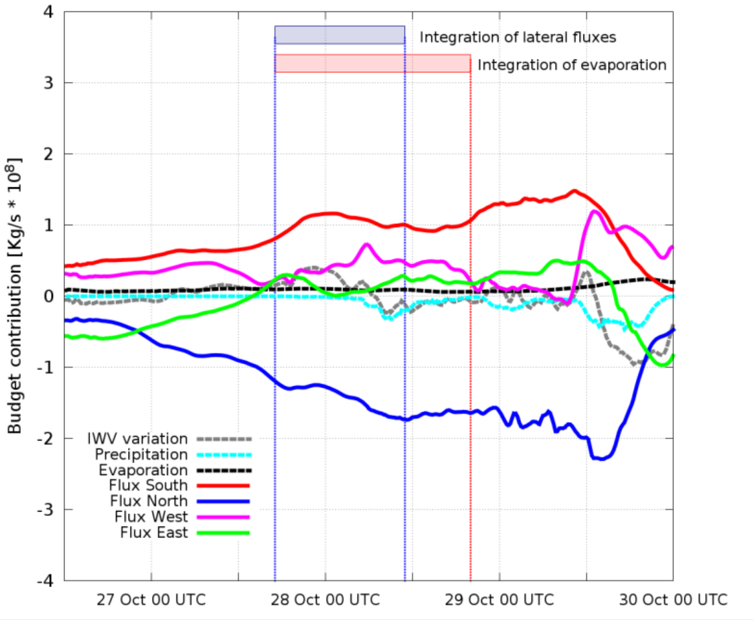

FIG. 9. As in Fig. 8 but for precipitation over central Italy within the box shown in Fig. 7c.

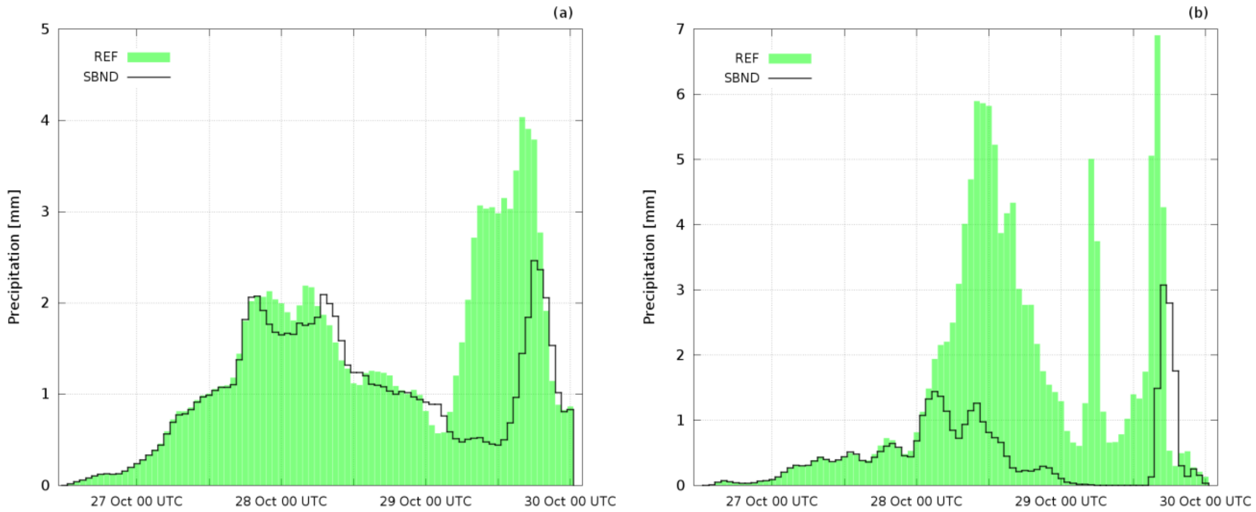

FIG. 10. Area-averaged hourly precipitation over (a) the northern and (b) the central Italy area. Green histograms for the reference simulations, black solid line for the sensitivity experiments (SBND) with reduced moisture across the southern boundary.

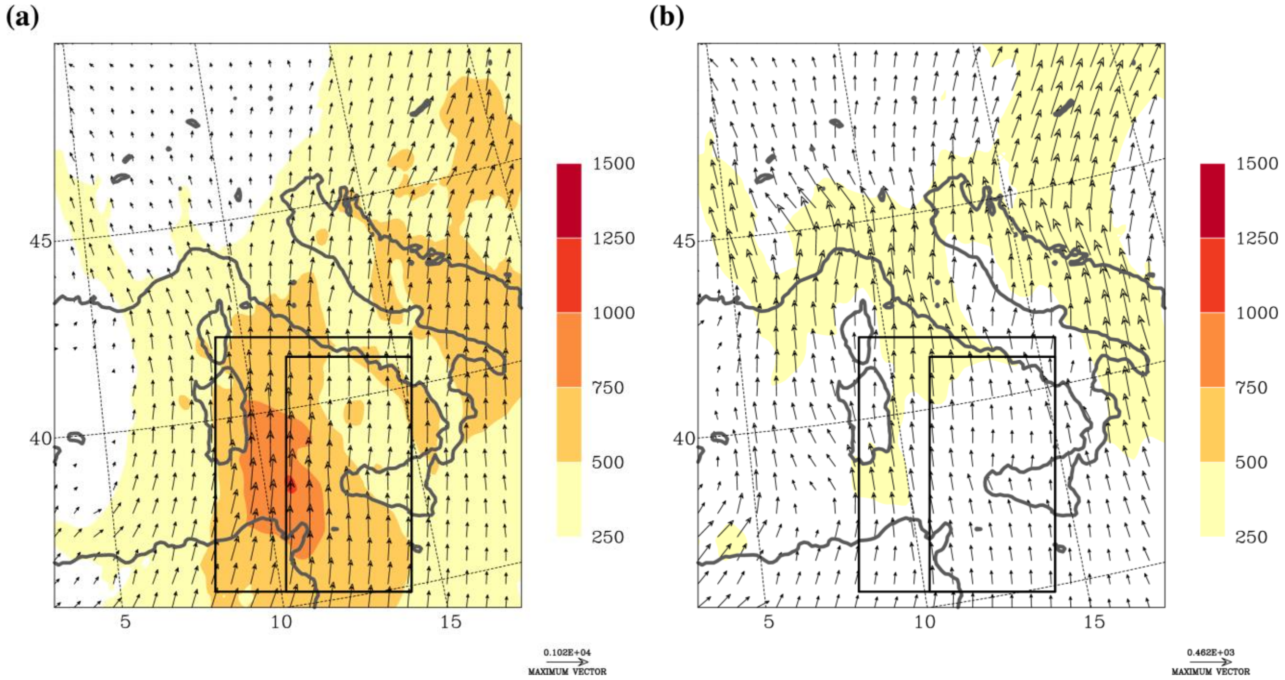

Fig. 11. Integrated Vapor Transport (kg m^{-1} s^{-1}, color shading and arrows) at 0000 UTC, 29 Oct. 2018 for (a) the reference simulation (REF) and (b) the sensitivity experiments (SBND) with reduced moisture across the southern boundary. The two boxes (shown also in Figs. 7a,c) used to compute the atmospheric water budget concerning rainfall over northern Italy (larger box) and central Italy (smaller box) are also plotted.

981

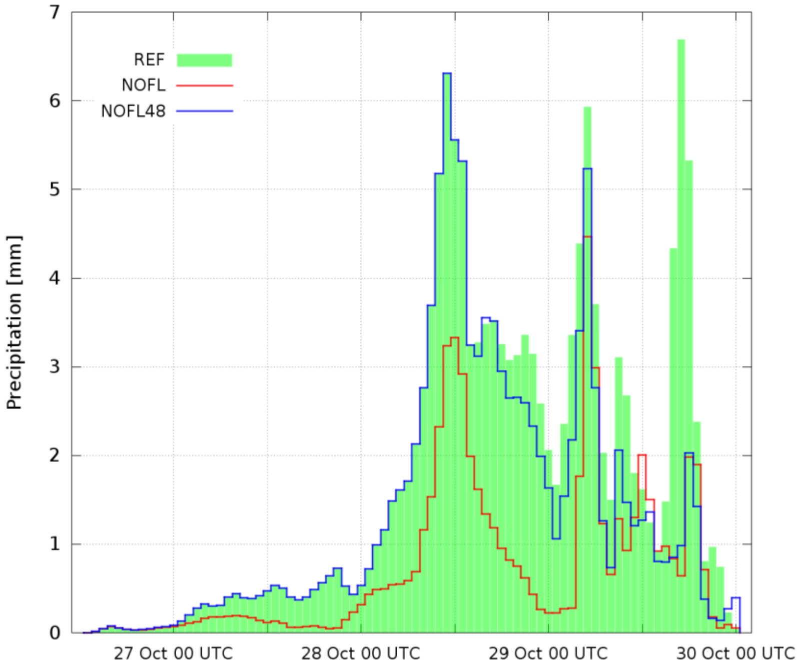

982

983

984 FIG. 12. Area-averaged hourly precipitation over the central Italy area. Reference simulation (REF, green histograms),

985 and the two sensitivity experiments without evaporation from the sea since the beginning (NOFL, black solid line) and

986 after 48 h of simulation (NOFL48, red solid line).

987

Fig.1a

Click here to access/download

Non-Rendered Figure

01a.tiff

Fig.1b

Click here to access/download

Non-Rendered Figure

01b.tiff

Fig.1c

Click here to access/download

Non-Rendered Figure

01c.tiff

Fig.1d

Click here to access/download

Non-Rendered Figure

01d.tiff

Fig.2a

Click here to access/download
Non-Rendered Figure
02a.tiff

Fig.2b

Click here to access/download
Non-Rendered Figure
02b.tiff

Fig.3

Click here to access/download
Non-Rendered Figure
03.png

Fig.4

Click here to access/download
Non-Rendered Figure
04.tiff

Fig.5a

Click here to access/download

Non-Rendered Figure

05a.tiff

Fig.5b

Fig.5c

Click here to access/download

Non-Rendered Figure

05c.tiff

Fig.5d

Click here to access/download

Non-Rendered Figure

05d.tiff

Fig.5e

Click here to access/download

Non-Rendered Figure

05e.tiff

Fig.5f

Click here to access/download

Non-Rendered Figure

05f.tiff

Fig.5g

Click here to access/download

Non-Rendered Figure

05g.tiff

Fig.5h

Click here to access/download

Non-Rendered Figure

05h.tiff

Fig.5i

Click here to access/download

Non-Rendered Figure

05i.tiff

Fig.6a

Click here to access/download

Non-Rendered Figure

06a.tiff

Fig.6b

Click here to access/download

Non-Rendered Figure

06b.tiff

Fig.7a

Click here to access/download
Non-Rendered Figure
07a.png

Fig.7b

Click here to access/download
Non-Rendered Figure
07b.png

Fig.7c

Click here to access/download
Non-Rendered Figure
07c.png

Fig.7d

Click here to access/download

Non-Rendered Figure

07d.png

Fig.8a

Click here to access/download

Non-Rendered Figure

08a.png

Fig.8b

Click here to access/download

Non-Rendered Figure

08b.png

Fig.9

Click here to access/download
Non-Rendered Figure
09.png

Fig.10a

Click here to access/download
Non-Rendered Figure
10a.png

Fig.10b

Click here to access/download

Non-Rendered Figure

10b.png

Fig.11a

Click here to access/download

Non-Rendered Figure

11a.tiff

Fig.11b

Click here to access/download
Non-Rendered Figure
11b.tiff

Fig.12

Click here to access/download
Non-Rendered Figure
12.png